Ore Geology Reviews 94 (2018) 396–413

Contents lists available at ScienceDirect

Ore Geology Reviews

journal homepage: www.elsevier.com/locate/oregeorev

Geochemical investigation of the lower Cambrian mineralised black shales of South China and the late Devonian Nick deposit, Canada

Anais Pagès[a,*], Steve Barnes[a], Susanne Schmid[a], Raymond M. Coveney Jr.[b], Lorenz Schwark[c,d], Weihua Liu[e], Kliti Grice[c], Haifeng Fan[f,g], Hanjie Wen[f,g]

[a] CSIRO Mineral Resources, 26 Dick Perry Avenue, Kensington, WA 6151, Australia
[b] Department of Geosciences, University of Missouri, Kansas City, MO 64110-2499, USA
[c] WA Organic and Isotope Geochemistry Centre, Department of Chemistry, The Institute for Geoscience Research, Curtin University, GPO Box U1987, Perth, WA 6845, Australia
[d] Institute of Geoscience, Kiel University, Ludewig-Meyn Str. 10, 24118 Kiel, Germany
[e] CSIRO Mineral Resources, Clayton, VIC 3168, Australia
[f] State Key Laboratory of Ore Deposit Geochemistry, Institute of Geochemistry, Chinese Academy of Sciences, Guiyang 550002, Guizhou, China
[g] University of Chinese Academy of Sciences, Beijing 100049, China

ARTICLE INFO

Keywords:
Nitutiang Formation
China
Nick deposit
Canada
Polymetallic shale
Geochemistry

ABSTRACT

Lower Cambrian (Tommotian) black shales of the Niutitang Formation, South China, host a thin accumulation (5–20 cm) of Ni, Mo, platinum group elements (PGE)-Au, Ni, As, Zn, Cu, V and rare earth elements (REE). Of all known deposits, the late Devonian Ni-Mo-PGE sulphide horizon in black shales of the Nick deposit, Selwyn Basin in Canadian Yukon, presents the strongest similarity with the Niutitang Formation polymetallic layer. In the present study, samples of the mineralised layer and host shales in South China from two mine sites (Zunyi and Sancha) were investigated in order to further characterise the prevailing redox conditions and mechanisms involved in the metal concentration process at both sites. Additional comparison with the Nick deposit mineralised layer was also undertaken. Bulk geochemical analysis (including PGE analysis) were conducted on all samples, along with μm-scale investigation of metal distributions and associations by X-ray fluorescence (XRF) mapping and Synchrotron XRF mapping. The comparison of the two sites from South China highlights strong similarities in metal enrichment factors. PGE and REE distribution patterns are also highly similar and suggest a source from seawater. Strong variations in elemental distributions at μm-scale were observed at both sites, most likely related to intense variations in redox conditions in the sediment. The comparison with the Nick deposit highlights a stronger enrichment in Ni and Zn in the Nick deposit and a greater variety of minerals in the Niutitang shales. The PGE and REE distributions of both the Nick deposit and the Niutitang shales, however, present highly similar patterns, and support an origin from seawater. The present study provides further insight into mineralisation style and processes in these mineralised black shales, highlighting the importance of redox conditions and re-emphasizing the role of organic matter in the formation of these mineralised layers.

1. Introduction

Black shales are commonly host to large Zn-Pb deposits; however, rare Ni-Mo-PGE enriched sulphide beds have been reported in the Cambrian shales of South China (e.g. Coveney and Nansheng, 1991; Jiang et al., 2006) and Devonian shales of the Yukon, Canada (Goodfellow, 2007). The sediment-hosted mineralisation of South China is found in lower Cambrian (Tommotian) black shales of the Niutitang Formation. This mineralised layer, corresponds to a thin accumulation (5–20 cm) of Ni, Mo, Au, Ag, Se, Cr, V, Zn, U, rare earth elements (REE) and platinum group elements (PGE) that can be traced along the same stratigraphic horizon over distances up to 2000 km (Mao et al., 2002). Despite the fact that mineralised horizons have been detected hundreds of km apart, it remains unclear whether this ore body forms a continuous layer across South China. In addition, the origin of these deposits remains highly controversial with studies supporting a hydrothermal origin and other supporting a seawater scavenging mechanism (e.g., Coveney and Nansheng (1991), Orberger et al. (2007), Pi et al. (2013), Lehmann et al. (2016)).

For instance, Coveney and Nansheng (1991) conducted a study of the mineralised layer with SEM/EDS, PGE and S isotope analysis and proposed an origin from submarine springs, mentioning that some

* Corresponding author.
E-mail address: Anais.pages@csiro.au (A. Pagès).

https://doi.org/10.1016/j.oregeorev.2018.02.004
Received 23 October 2017; Received in revised form 23 January 2018; Accepted 2 February 2018
Available online 03 February 2018

metals could have potentially been added during a second stage of mineralisation via circulating basinal brines. Murowchick et al. (1994) reported $\delta^{34}S$ values ranging from +22 to −26‰ for sulphide nodules attributed to the activity of bacterial sulphate reduction. The authors proposed that the ore genesis took place in an anoxic, phosphogenic and metallogenic basin with intermittent venting of metal-rich hydrothermal fluids. Li and Gao (1996) detected positive Eu anomalies in cherts interbedded with the black shales of the Niutitang Formation and proposed a hydrothermal origin for these cherts. Lott et al. (1999) performed fluid inclusion measurements on quartz-sulphide stock work found about 10 m below the mineralised horizon. The temperatures up to 290 °C suggested that hydrothermal fluids leaked through stock work veins, supplying metals to the seafloor. Steiner et al. (2001) suggested that the positive Eu anomaly detected within the mineralised layer and immediate footwall black shales highlighted a possible origin from groundwater seeps. Jiang et al. (2006) performed TE, REE and Pb isotopic analysis on the ore body and adjacent shales. Comparison of Ce and Y anomalies and Y/Ho between non-mineralised shales and the ore body suggested a hydrothermal origin. Orberger et al. (2007) conducted a comprehensive study that included TE, REE and PGE analysis, TEM and Raman spectroscopy. The authors proposed that hydrothermal fluids (between 250 and 300 °C) enriched in Fe, Ni, Se, Zn, Cu, Pb, Pd, Pt and Si leached from an underlying mafic–ultramafic basement and were further enriched in Ba, Ca, Mg and P during percolation through phosphorite, barite and dolomite. Kříbek et al. (2007) performed a thorough characterisation of the organic matter present in the ore body. This study reported the presence of migrabitumens and organic remnants of oncolite-like algal bodies living in shallow oxic environment and later transported to deep anoxic waters. The authors suggested that metals could have been scavenged from seawater or trapped onto organic matter, however, a possible enrichment from low-temperature hydrothermal fluids was also proposed. In addition, Pašava et al. (2008) proposed that this ore layer represents the remnants of a shallow-water metal-rich hardground horizon formed in a semi-restricted, sediment deprived basin. The authors suggested a mixed origin for the metals with Ag, Cr, Ce, Ni, PGE, Sb, Zn and V deriving from hydrothermal fluids and Mo and P originating from seawater. Finally, Pi et al. (2013) reported Mo/TOC ratios up to 3000, Ni/TOC up to 3912 and U/TOC up to 14 and proposed a hydrothermal enrichment to explain these anomalously elevated ratios.

Mao et al. (2002), however, proposed a seawater scavenging origin for the mineralised layer. The authors argued that sedimentary exhalative (SEDEX) deposits commonly contain a Cu-Pb-Zn assemblage, differing from the one observed in the Niutitang layer. In addition, it was mentioned that the remarkably wide lateral extent of the metalliferous sulphide layer, only a few cm thick, over hundreds of km, did not coincide with a common source from hydrothermal brine. This study also highlighted that the mineralised horizon contained consistent enrichment factors to that of seawater, on the order of 10^6 to 10^8, for Au, Ag, Re, Se, V, As, Sb, Co, Pb, Hg, Re, W, Sb, Zn, Ni, Mo and PGE. The authors proposed an origin from seawater in a stagnant basin with very low sedimentation rate and replenishment by fresh seawater at a time scale of hundreds of years. Lehmann et al. (2007) also argued for a similar origin, proposing that the Yangtze Platform had a particular paleogeographic situation allowing the presence of coastal upwelling promoting high surface productivity and maintaining an oxic layer above a sediment-starved euxinic basin. Mo isotope ratios reported in this study also suggested that sub-oxic to anoxic marine environments were more widespread during the Early Cambrian than in modern environments. Lehmann et al. (2016) further suggested that mineralisation deriving from groundwater seeps would present a varying isotopic composition in Cr, Mo and Os along the continental margins related to different groundwater flow paths and would not show concentrations in Mo, Re or Ni greater than seawater. As highlighted by Lehmann et al. (2007), data previously obtained from the Niutitang mineralised horizon do not support such origin from groundwater seeps. Intraformational basinal fluids can potentially form U mineralisation also enriched in Mo, Ni, V, REE, Au and PGE such as the mineralisation observed in the Key Lake and McArthur River U deposits in Canada (Lehmann et al., 2016). Nonetheless, the authors argued that the strictly stratiform characteristics of the ore body and the homogeneity in various isotopic patterns did not coincide with such origin. In addition, the Cr isotope data strongly supported a seawater metal source with metals being derived from oxidative weathering of the continents (Lehmann et al., 2016). Finally, the authors also argued that a possible origin from petroleum discharge could not account for PGE and Re enrichments as Re and Os have a low affinity for oil phases. An additional study conducted by Xu et al. (2013) emphasized that the PGE ratios of the polymetallic sulphides are similar to those of modern day seawater but do not resemble classical hydrothermal values; hydrothermal concentrations of PGEs typically have high ratios of Pd to all other PGEs, and characteristically low Os, Ir, Ru and Rh (Barnes and Liu, 2012 and references therein). The authors also suggested that elemental concentrations coincide with present day seawater concentrations with an enrichment factor of 10^7, much different from hydrothermal sulphides. The pronounced positive Y anomaly was also proposed to confirm a seawater scavenging origin. A recent study by Yin et al. (2017) on Hg isotopes also supported a metal source from seawater, based on the positive Δ^{199} Hg and Δ^{200} Hg values. The authors proposed that the organic matter decay and remineralization under anoxic to euxinic conditions, along with very low clastic input, promoted the metal enrichment.

One of the reasons for the wide diversity of models and interpretations of the Niutitang mineralized black shale occurrence is the extreme rarity of this type of deposit, and the consequent lack of a basis for comparison. Of all the few known deposits of this type, the Ni-Mo-PGE sulphide horizon in black shales of the Late Devonian Nick deposit, Selwyn Basin (Yukon, Canada) presents the strongest similarity with the Niutitang Formation polymetallic layer (Coveney and Nansheng, 1991). The mineralised layer in the Nick deposit varies between 5 and 15 cm in thickness, extends over a strike length of more than 400 km and contains abundant Ni, Mo, PGE and Au (Goodfellow, 2007). In many respects, it is a direct analogue of the Niutitang mineralised layer but has been much less studied, aside from a few studies that investigated the mineralogy (e.g. Goodfellow, 2007; Hulbert et al., 1992; Orberger et al., 2003).

The main goal of the study presented here is to evaluate competing genetic models for polymetallic black shale mineralisation by making two comparisons on the basis of geochemistry and detailed element distributions: firstly between two widely separated Niutitang locations, Zunyi and Sancha, located 600 km apart, in order to further characterise the prevailing redox conditions and mechanisms involved in the metal concentration processes at both sites; and secondly, comparing these localities with the Nick deposit as a basis for testing hypotheses across two different deposits of significantly different age. A novel aspect of the present study is a μm-scale investigation of metal distributions and associations by X-ray fluorescence (XRF) mapping and Synchrotron XRF mapping in samples from Zunyi, Sancha and the Nick deposit. This study emphasizes the role of redox conditions in the formation of these deposits. As well as focussing on the similarities and differences identified between two sites located hundreds of km apart in South China, this study offers for the first time a direct comparison with a similar deposit of a different age on a different continent, providing an opportunity to note commonalities and differences between these highly unusual mineralised black shales.

2. Geological setting

2.1. Metalliferous black-shales of South China

Cambrian sedimentary rocks are widely exposed in the Yangtze Platform of South China. The Cambrian facies represent a depositional

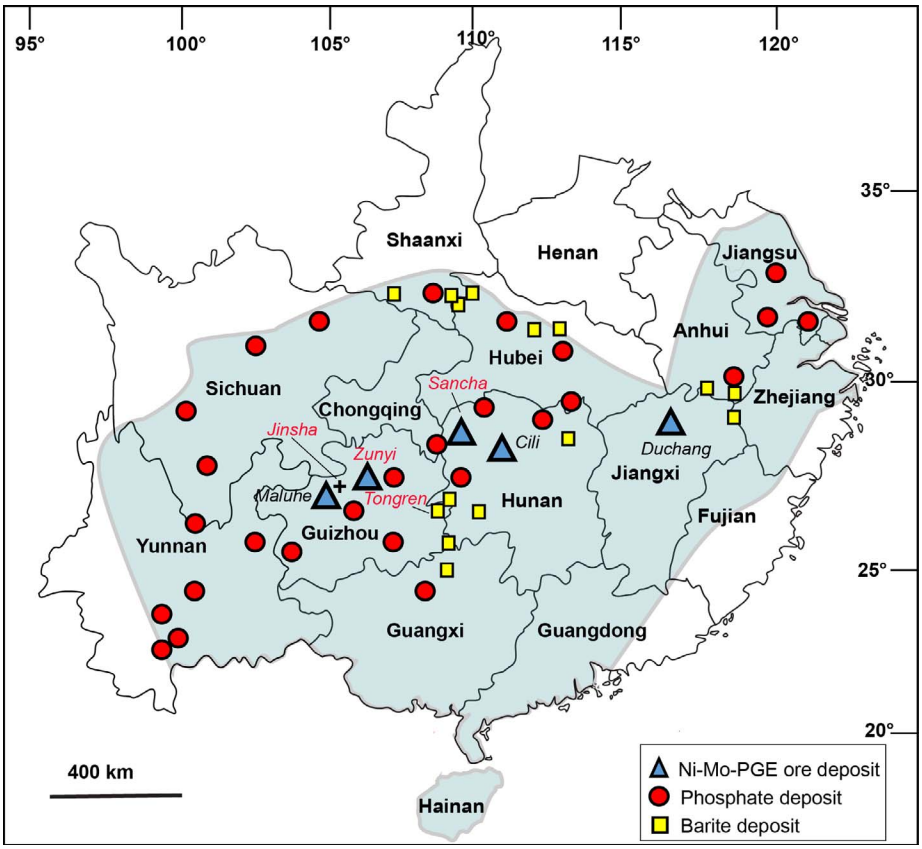

Fig. 1. Map of the Yangtze Platform, China. The blue triangles indicate the locations where the mineralised layer has been reported, including Zunyi and Sancha (modified from Jowitt and Keays, 2011). (For interpretation of the references to colour in this figure legend, the reader is referred to the web version of this article.)

shift from a shallow shelf environment with phosphatic carbonate rocks in the northwest to a protected and deep basinal facies of black shale in the southeast (Zhu et al., 2003).

The Niutitang Formation unconformably overlies the Ediacaran Dengying Formation (551–541 Ma). The Niutitang Formation is mainly composed of highly organic rich black shales containing phosphatic beds and tuff layers. A polymetallic Ni–Mo–PGE–Au sulphide ore layer, with a thickness varying between 5 and 20 cm, although it locally extends up to 2 m at the Huangjiawan mine in Zunyi (Zeng, 1998), is present locally in the lowermost part of the Niutitang Formation. Samples from Zunyi and Sancha (Fig. 1) were analysed in this study.

This mineralised layer, with a Re–Os age of 521 ± 5 Ma (Xu et al., 2012) is found along a 2000-km long narrow NE striking belt of transitional and deeper water facies, along the margins of the Yangtze platform (Mao et al., 2002). Phosphorites can be observed locally in the Lower Niutitang Formation. Thicknesses of phosphorite beds vary between 0.3 and 1.35 m with P_2O_5 grade of 10.6–33.4 wt%.

The ore layer is extremely enriched in Mo, Ni, Se, Re, Os, As, Au, Hg, Sb, Ag, Pt, and Pd, on the order of 10^6–10^9 in comparison with seawater concentrations (Mao et al., 2002; Murowchick et al., 1994; Steiner et al., 2001). In comparison to average upper continental crust (Taylor and McLennan, 1985), metals such as Mo, Ni, Se, Re, Os, As, Hg, and Sb are enriched on the order of 10^4, and metals such as Ag, Au, Pt, and Pd are enriched on the order of 10^3 (Mao et al., 2002). The mineralised layer can have a narrow lenticular, and bedded or nodular shape and is consistently found in the lowermost Niutitang Formation. The ore layer contains a complex mixture of nanocrystalline molybdenite (MoS_2), vaesite, bravoite, jordisite, arsenopyrite, chalcopyrite, covellite, sphalerite, millerite, polydymite, gersdorffite, sulvanite, pentlandite, tennantite, tiemannite, violarite, and native Au (Coveney et al., 1994; Kao et al., 2001; Lott et al., 1999). Nodules (1–3 mm) contain a heterogeneous assemblage of Ni–Mo sulphides, a colloid-like Mo–S–C phase associated with organic matter and phosphorites. The high thermal maturity of the bulk organic matter corresponds to semi-anthracite to anthracite coalification stage (Kříbek et al., 2007).

2.2. The Nick deposit

Of all known deposits, the Ni-Mo sulphide beds of the Devonian Nick deposit in the Selwyn Basin, Yukon, Canada, present the strongest similarities with the South China black shales (Coveney and Nansheng, 1991; Fig. 2). Similar to the metal-rich Niutitang shales, the Nick deposit is characterised by a thin mineralised layer deposited within a black shale succession, immediately overlying a carbonate platform sequence. The mineralised horizon is conformable and is found at the base of the Devonian–Mississippian Earn Group, at the contact between the Lower and Middle Devonian sedimentary succession (Hulbert et al., 1992). This sedimentary sequence overlies the Cambro-Ordovician carbonate rocks of the Mackenzie platform, the continental margin of the Selwyn Basin (Hulbert et al., 1992). The Selwyn Basin was a large, rift-controlled, at times anoxic basin extending from Alaska to British Columbia through the Yukon and the Northwest Territories (Goodfellow, 2007). The orebody was deposited at the transition zone from shallow to deep marine environments (Hulbert et al., 1992).

Although the age of mineralisation has not been constrained yet for the Nick deposit, conodonts from limestone clasts a few meters below the mineralisation appear to be mid- to late-Emsian to Eifelian in age while radiolarians from cherts found 40 cm above the mineralised layer suggest a Frasnian age. Therefore, it seems that the mineralisation could be slightly older than the Frasnian-Famennian mass extinction event (Goodfellow, 2007).

The thickness of the mineralised Nick layer varies between 5 and 15 cm and contains abundant Ni (7.8% Ni), Zn (1.2%), Mo (0.4%) and PGE (up to 1050 ppb). This layer is mainly composed of pyrite, vaesite,

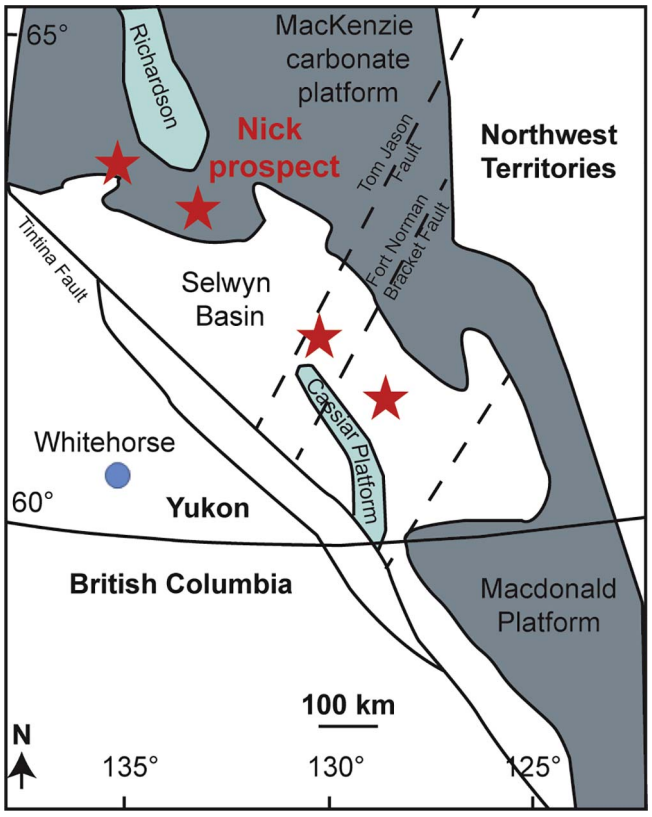

Fig. 2. Map of the Selwyn Basin, Canada. The red stars indicate locations where the mineralised horizon has been reported, including the Nick deposit (modified from Jowitt and Keays (2011). (For interpretation of the references to colour in this figure legend, the reader is referred to the web version of this article.)

melnikovite (sulphide "gel" of pyrite and marcasite), wurzite and sphalerite (Hulbert et al., 1992). The Nick deposit also preserves plant material suggesting an input of terrestrial material. An affinity with SEDEX mineralisation has been suggested (Hulbert et al., 1992).

3. Methods

3.1. Sampling sites and outcrop descriptions

The Jinsha section is located 90 km from Zunyi city, Guizhou Province. The succession includes rock units from the Dengying Formation, the Niutitang Formation and the Mingxinsi Formation. No Ni–Mo–PGE ore layer was present in this section.

The Dazhuliushui Ni–Mo–PGE ore layer is located about 26 km from Zunyi city, Guizhou Province. Neoproterozoic units of the Nantuo, Doushantuo and Dengying Formations, and black shale of the Cambrian Niutitang Formation are exposed. The Ni–Mo–PGE sulphide ore deposit is located between 5 and 8 m above the contact with the Dengying Formation.

The Sancha Ni–Mo–PGE ore layer in Hunan Province is located about 380 km northeast of the Dazhuliushui mine site. At this site, the Niutitang Formation disconformably rests on the Dengying Formation. The lowermost part of the section includes bedded and nodular phosphate. The sulphide ore layer is about 1 m above the unconformity with the dolostones of the Dengying Formation.

Outcrop sampling was conducted at three different sites: Jinsha, Zunyi and Sancha. A total of fourteen samples were collected at the Zunyi section. The sampled section comprises the mineralised layer from the lowermost Niutitang Formation, including host shale, pyrite nodules, chert, phosphorite bed and dolostone of the Dengying Formation. Fifteen samples were collected at the Sancha section

Fig. 3. Photograph of the mineralised layer in Zunyi.

incorporating the mineralised layer (Fig. 3), surrounding host shales and phosphorites of the Niutitang Formation. Eight samples were collected at the Jinsha section, including the dolostones of the Dengying Formation, black shale of the Niutitang Formation and siltstone and limestone of the Mingxinsi Formation.

An outcrop sample (5 × 10 cm) of the mineralised horizon of the Nick deposit, Canada was collected in order to compare geochemistry and microstructures from the South China shales and from the Nick deposit. This sample was taken from a natural outcrop at the base of the Lower Earn Group, located around 100 km north of Keno City, Yukon Territory, Canada. This outcrop was the only one that could be easily accessed by helicopter during the summer field season.

3.2. Whole rock geochemistry

Multi-element assay on 37 whole-rock pulps was performed at Intertek laboratories in Perth using a multi-acid (HNO_3–$HClO_4$–HF–HCl) digest, and ICP-OES/MS analysis. Elements analysed were Ag, Al, As, Ba, Be, Bi, Ca, Cd, Ce, Co, Cr, Cs, Cu, Dy, Eu, Fe, Ga, Gd, Hf, Ho, In, K, La, Li, Lu, Mg, Mn, Mo, Na, Nb, Nd, Ni, P, Pb, Pr, Rb, Re, S, Sb, Sc, Se, Sm, Sn, Sr, Ta, Tb, Te, Th, Ti, Tl, Tm, U, V, W, Y, Yb, Zn, Zr. Major oxides, including SiO_2, Al_2O_3, Fe_2O_3, CaO, MgO, Na_2O, K_2O, MnO, TiO_2, P_2O_5, Cr_2O_3 and Ba, were analysed by XRF. Selected samples (3 pulps) were further analysed by for nickel sulphide fire assay in order to obtain Au, Ir, Pt, Pd, Re, Os concentrations.

3.3. TOC measurements and Rock-Eval pyrolysis

Rock-Eval pyrolysis was used to estimate the hydrocarbon potential of rock samples by open system volatilisation and cracking of organic matter according to a programmed temperature pattern. The pyrolyzed hydrocarbons are monitored by a flame ionization detector (FID), forming the so-called peaks S1 (thermovaporized free hydrocarbons), S2 (pyrolysis products from cracking of organic matter) and S3 (CO_2 released during the pyrolysis).

Decalcification of ground samples was achieved by using HCl (6 M) to remove calcium carbonate. Aliquots of dried residues (50 °C, 72 h) were subject to standard organic geochemical analysis: a ROCK-EVAL II PLUS analyser (Vinci technologies) was used to determine the hydrogen index (HI) a Vario CNS-Elemental Analyser (Elementar®) was employed to estimate the total carbon content of the decarbonated samples. The carbonate content was estimated based on the weight loss related to carbonate dissolution by HCl. Bulk organic geochemical analyses were run in duplicate or triplicate when possible and standards were run every 10 samples.

3.4. Petrographic study

Thin sections (30 µm thick) were prepared focusing on the mineralised layers. These samples were studied by optical and scanning electron microscope (SEM). Optical images were obtained with a Nikon ore microscope. Backscattered electron images obtained with a Zeiss Ultra-Plus FEG-SEM coupled with a Bruker X-Flash energy dispersive X-ray spectroscopy (EDS) detector for elemental analyses. An accelerating voltage of 20 kV in high current mode was used.

3.5. Desktop microbeam XRF mapping

X-ray fluorescence (XRF) elemental mapping was performed using a Bruker Tornado™ desktop equipped with a rhodium target X-ray tube operating at 50 kV and 500nA without filters and an XFlash® silicon drift X-ray detector. Beam diameter and point spacing of 40 µm was routinely for optimal map resolution, with dwell times varying from 3 to 10 ms depending on sample size. These elemental maps allow 2-D visualisation of the spatial variations in major and few minor elements.

3.6. Synchrotron-based microbeam XRF mapping

XRF microscopy was performed on a subset of samples at the XFM beamline at the Australian Synchrotron in Melbourne using the Kirkpatrick Baez mirror microprobe end-station. This provides a monochromatic 2 µm beam-spot size for energies in the range 4–20 keV. Equipped with the Maia 384 detector array, the XFM beamline can acquire data at 2 µm resolution from 384 detectors simultaneously over areas of several square centimetres with count rates of ~4–10 M/s, energy resolution of 300–400 eV. These spectra are then processed by the GeoPIXE software into element concentrations represented as maps of quantified element concentrations based on standardless correction of raw count data (Kirkham et al., 2010; Ryan et al., 2010).

4. Results

4.1. Barren section: Jinsha

Samples collected along the Jinsha section contain up to 116 ppm of As (average 20 ppm), 142 ppm of Cu (average 49 ppm), 134 ppm of Mo (average 22 ppm), 59 ppm of Ni (average 29 ppm), 194 ppm of U (average 29 ppm), 1781 ppm of V (average 338 ppm), 348 ppm of Zn (average 109 ppm) and TOC varying between 0.1 and 6 wt% (Fig. 4). Rock Eval pyrolysis shows S1 values ranging between 0.1 and 0.4 mg/g rock, S2 not detectable and S3 ranging between 0.1 and 3.2 mg/g rock. Analytical results are presented in Table 1.

4.2. Mineralised sections

4.2.1. Whole rock geochemistry and Rock-Eval pyrolysis

4.2.1.1. Sancha. Samples collected along the Sancha section contain up to 74 ppm of As (average 44 ppm), 125 ppm of Cu (average 63 ppm), 186 ppm of Mo (average 128 ppm), 215 ppm of Ni (average 158 ppm), 78 ppm of U (average 53 ppm), 1045 ppm of V (average 544 ppm), 313 ppm of Zn (average 190 ppm) and 14 wt% TOC (Fig. 5) in the non-mineralised succession and is similar to Jinsha. Rock Eval pyrolysis shows S1 values ranging between 0.2 and 0.8 mg/g rock, S2 not detectable and S3 ranging between 0.2 and 0.7 mg/g rock. The mineralised horizon (~ 5 cm thick) contains concentrations of 3642 ppm As, 565 ppm Cu, 10,223 ppm Mo, 5941 ppm Ni, 530 ppm U, 1864 ppm V, 363 ppm Zn, 7 wt% TOC and S1 value of 0.3 mg/g rock and S2 of 0.4 mg/g rock. The phosphorite layer underneath the polymetallic horizon contains 49 ppm As, 81 ppm Cu, 130 ppm Mo, 77 ppm Ni, 178 ppm U, 306 ppm V, 29 ppm Zn, 8 wt% TOC, S1 of 0.3 mg/g rock and S3 of 0.3 mg/g rock. Analytical results are presented in Table 1.

4.2.1.2. Zunyi. Samples collected along the Zunyi section contain up to 320 ppm of As (average 65 ppm), 156 ppm of Cu (average 65 ppm), 300 ppm of Mo (average 66 ppm), 539 ppm of Ni (average 149 ppm), 261 ppm of U (average 41 ppm), 1029 ppm of V (average 307 ppm), 818 ppm of Zn (average 210 ppm) and 11 wt% TOC (Fig. 6) in the non-mineralised succession. Rock Eval pyrolysis shows S1 values ranging between 0.0 and 1.0 mg/g rock, S2 not detectable and S3 ranging between 0.1 and 1.5 mg/g rock. The mineralised horizon contains concentrations of 2594 ppm As, 2256 ppm Cu, 11,875 ppm Mo, 13,735 ppm Ni, 167 ppm U, 757 ppm V, 1248 ppm Zn, 0.4 wt% TOC, S1 of 0.1 mg/g rock and S3 of 0.2 mg/g rock. Analytical results are presented in Table 1.

4.2.2. Enrichment factors

As the Jinsha section does not present any mineralised interval, it is used as a reference for comparison with other sections that show mineralised horizons. The sample 4 (Niutitang Formation), in particular, presents a typical non-mineralised black shale composition and was chosen as a reference sample to evaluate the enrichment factors of mineralised black shales from other sections. Multi-element spidergrams of concentrations normalised to the ones in Jinsha are presented in Fig. 7.

The samples from the Sancha section all show anomalous concentrations in Ag (3–10 enrichment factor (EF)), As (8–16 EF), Cu (31–125 EF), Mo (20–29 EF), Ni (2–4 EF), Se (12–30 EF), U (5–10 EF), V (1–3 EF), Zn (1–5 EF). Of all the un-mineralised samples, the sample Sa2 (30 cm above the mineralised layer) presents the greatest enrichment in Ag, As, Cu and Se. P is only very slightly enriched in comparison with the barren shale with an enrichment factor ranging between 0.3 (Sa10) and 1 (Sa2). The mineralised layer shows greater enrichments factors in Ag (39 EF), As (520 EF), Cu (52 EF), Mo (816 EF), Ni (111 EF), Se (1248 EF), U (75 EF) and V (19 EF). P is also much more abundant (30 times enriched) than in the other samples. Zn, however, is not particularly enriched (1.5 EF).

The mineralised layer in Zunyi is enriched in Ag (244 EF), As (741 EF), Cu (223 EF), Mo (2423 EF), Ni (305 EF), Se (1639 EF), U (22 EF) and V (2 EF). Thus, the mineralised horizon in Zunyi is more enriched in Ag, As, Cu, Mo and Ni but less enriched in V and U than the mineralised layer in Sancha. P shows a highly similar enrichment in both layers (31 EF in Zunyi versus 30 EF in Sancha). Zn, however, is more enriched in Zunyi (21 EF) than in Sancha (1.5 EF).

The Nick deposit is enriched in Ag (34 EF), As (947 EF), Cu (38 EF), Mo (652 EF), Ni (1344 EF), Se (111 EF), U (9 EF), V (2 EF) and Zn (165 EF). P, however, is not enriched, in comparison to the barren shale.

4.2.3. PGE distributions

Analytical results are presented in Table 2 and PGE distribution patterns of Zunyi, Sancha, the Nick deposit and modern seawater are presented in Fig. 8. Samples from the mineralised horizon in Zunyi and Sancha both show a very similar distribution of PGEs. The Nick deposit also shows a highly similar pattern to the China samples, as previously observed by Lehmann et al. (2016), who compared samples from Zunyi and the Nick deposit. PGE from all three sites show enrichment factors of about 4 orders of magnitude, in comparison with seawater. In addition, PGE distribution patterns in all three sites present a remarkably similar trend to seawater PGE distribution pattern.

Almost identical concentrations of Ir were measured in samples from the three sites: 3.5 ppb in Sancha and Zunyi and 3 ppb in the Nick deposit. Of all PGEs, Ir presents the lowest concentration in all three sites. Re concentrations reach 10 ppb in Zunyi, 5 ppb in Sancha and 31 ppb in the Nick deposit. Pd is the most abundant PGE in both Zunyi and Sancha with concentrations of 291 and 217 ppb, respectively, and Pt the second most abundant with 287 ppb in Zunyi and 183 ppb in Sancha. In the Nick deposit, Pt is the most abundant PGE with a concentration of 417 ppb and Pd the second most abundant with a content of 203 ppb. These concentrations are much greater than those measured

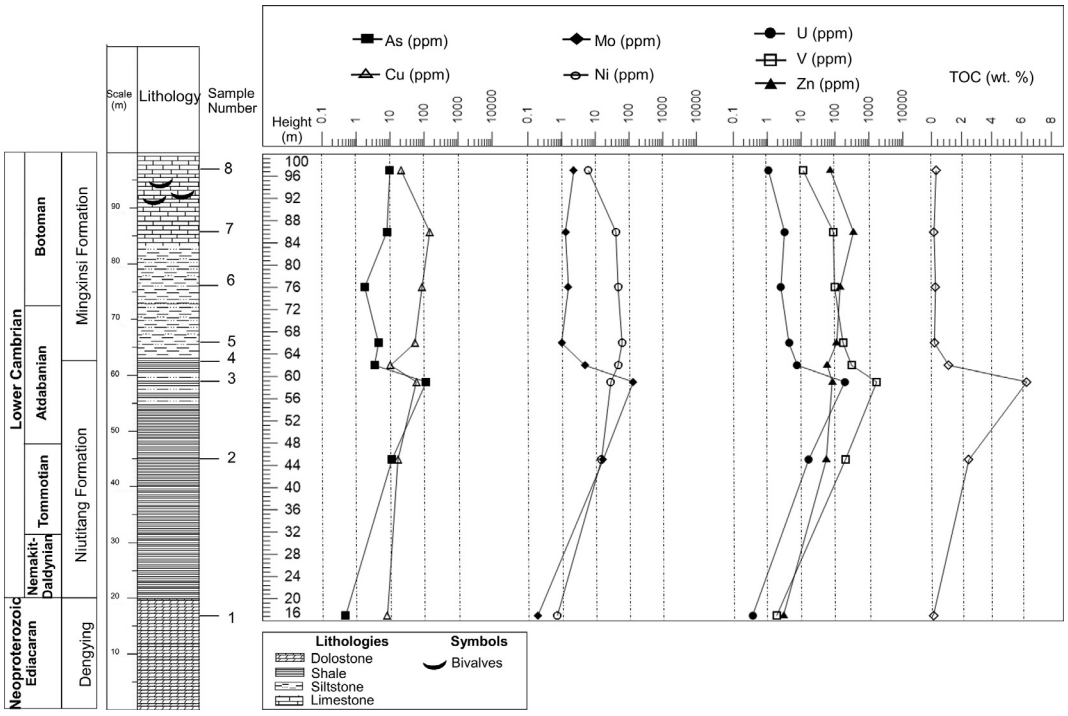

Fig. 4. Sedimentological log and As, Cu, Mo, Ni, U, V and Zn concentrations from the Jinsha samples.

in shales surrounding the mineralised layer in the Nick deposit: Pd concentrations between 0.81 and 4.5 ppb and Pt concentrations between 0.05 and 0.86 ppb (Hulbert et al., 1992; Pasăva, 1993).

4.2.4. REE patterns

The geochemical behaviour of the REE and Y can provide further understanding of the redox conditions and metal sources. Analytical results are presented in Table 3 and Fig. 9 highlights the distributions of REE and Y normalised to post-Archean Australian shales (PAAS) for the mineralised layer in Sancha and Zunyi, the Nick deposit, modern seawater and a sample from the Tokyo Bay (restricted environment) (Nozaki and Zhang, 1995).

The Sancha mineralised layer shows depleted light-REE and a positive Y anomaly. The Zunyi mineralised layer also presents depleted light-REE, a positive Y anomaly but also a slightly positive Eu anomaly. The Nick deposit sample shows depleted light-REE, a positive Y anomaly and a negative Ce anomaly. The modern-day seawater presents depleted light-REE, a positive Y anomaly and a strong negative Ce anomaly while the Tokyo Bay sample (restricted environment) also presents depleted light-REE but a less pronounced Ce anomaly and a positive Y anomaly.

4.2.5. Petrographic study

Samples from the mineralised layer in Zunyi (Fig. 10A and B) and Sancha (Fig. 10C and D) contain a high diversity of minerals including apatite, gersdorffite, millerite, abundant massive and framboidal pyrite, nickeliferous pyrite and dolomite. Wood material was detected in the Nick deposit sample (Fig. 10E and F). The replaced wood cells typically consist of framboidal to massive pyrite and vaesite (NiS_2). Pyrite dominates in the interiors of woody cells and vaesite forms the walls.

4.2.6. XRF mapping

Elemental maps of the Sancha and Zunyi mineralised layers and the Nick deposit are presented in Fig. 11.

Analyses of the mineralised horizon from Sancha and Zunyi revealed the presence of brecciated structures and fine-scale segregations of metals. Although the samples clearly present brecciated structures at microscopic scale, these structures are not detectable in outcrop where only a sulphide laminated bed containing phosphorite nodules is visible.

In the Zunyi sample, some layers show fine laminations of P, Ni, As, Mo and S. Other layers present brecciated textures of black shales with disrupted organic matter lenses, fragmented phosphorites and a high abundance of Ni and As-rich sulphide clasts. Zn and Cu are disseminated and appear to be associated with the organic matter-rich matrix. V is disseminated and mainly associated with organic-rich clays.

In the Sancha sample, two distinct beds are detected. One part of the sample contains greater abundance of sulphides and higher abundance of As and Cu. The second zone contains abundant phosphorite nodules and fragments associated with V-rich clay and Ni-rich lenses.

Both samples from the Niutitang Formation present brecciated textures with abundant phosphorite nodules and fragments. Zn and V are dispersed and associated with the organic matrix while As, for instance, shows a greater association with sulphides. Cu is dispersed and associated with the organic-rich matrix in the Zunyi sample while it is more abundant in the sulphide-dominated zone in the Sancha sample.

The Nick deposit sample shows fairly different distributions of Ni, As and Fe with elongated lenses of pyrite and As-rich phase surrounded by fine laminations of Ni. The Nick deposit sample does not appear as brecciated as the South China samples and P is much less abundant. V is particularly abundant in the section of the sample that is shaly. Zn and Cu are concentrated as fine laminations on the edge of sulphide lenses.

4.2.7. Synchrotron-based XRF mapping

Detailed synchrotron-based XRF maps further highlight the complexity of metal distributions in the China shales and the Nick deposit (Fig. 12). The samples from Zunyi and Sancha show highly similar metal distributions with brecciated textures, abundant presence of pyrite (as highlighted by Fe distributions) and disseminated As on the edge of phosphorite nodules. The Nick deposit sample, however, shows abundant lenses of pyrite and arsenopyrite surrounded by fine laminations of Ni.

Table 1
Ag, Al, As, Cu, Mo, Ni, P, Pb, Se, Ti, U, V, Zn and Zr concentrations (in ppm) from Zunyi, Sancha and the Nick deposit. TOC values are in wt%, S1 and S3 values are in mg/g rock.

Sample	Depth (m)	Lithology	Ag	Al	As	Cu	Mo	Ni	P	Pb	Se	Ti	U	V	Zn	Zr	TOC	S1	S3
Zunyi 1	1	Dolostone	0.4	3048.0	21.9	12.5	2.5	63.0	4022.0	7.3	1.4	190.0	4.7	152.0	388.0	7.1	0.3	0.1	0.2
Zunyi 2	1.3	Phosphorite layer	2.1	5700.0	12.6	50.1	7.0	21.6	142500.0	10.3	3.5	700.0	260.5	996.0	128.7	0.3	0.2	0.1	0.1
Zunyi 3	1.4	Black shale	1.6	96400.0	60.2	155.7	36.0	38.5	6540.0	43.8	291.4	1040.0	35.4	42.0	97.7	244.7	3.8	0.6	0.3
Zunyi 4	2.3	Chert	4.4	3700.0	12.3	38.1	21.8	22.8	620.0	4.5	13.8	160.0	4.7	280.0	20.9	7.9	4.6	0.3	0.2
Zunyi 5	3.3	Black shale rich in pyrite nodules	0.8	64000.0	21.8	105.4	45.7	156.1	660.0	16.5	6.8	3590.0	20.1	1029.0	192.3	96.9	2.1	0.1	0.2
Zunyi 6	3.5	Black shale rich in pyrite nodules	3.2	38700.0	49.8	129.8	31.5	322.5	390.0	90.4	33.4	1970.0	12.6	413.0	54.6	50.3	2.3	0.0	0.2
Zunyi 7	4.3	Black shale	1.4	3300.0	8.1	22.1	15.0	11.6	70300.0	4.4	1.4	410.0	29.3	68.0	818.2		0.3	0.1	0.5
Zunyi 8	4.5	Black shale	14.4	37700.0	146.4	75.9	48.8	44.6	3020.0	93.0	81.0	1860.0	12.8	97.0	35.8	62.4	9.3	0.8	0.4
Zunyi 9	4.7	Sulfide-rich layer	3.9	73000.0	320.0	51.6	300.0	206.5	310.0	42.1	23.0	4980.0	18.2	283.0	133.9	103.2	1.6	0.2	0.3
Zunyi 10	4.8	Black shale	0.6	15300.0	58.3	15.0	49.9	285.0	530.0	6.0	9.2	740.0	14.0	119.0	235.1	16.7	7.0	0.3	0.2
Zunyi 11	4.8	Calcareous shale	0.1	2052.0	4.5	71.4	11.2	22.5	85.0	3.6	1.0	88.0	4.6	10.0	28.0	2.2	10.8	1.0	1.5
Zunyi 12	4.9	Black shale	0.2	6040.0	31.9	15.8	44.5	199.8	21895.0	5.4	3.6	367.0	37.5	117.0	162.0	8.1	0.3	0.1	0.2
Zunyi 13	4.9	Ni-Mo-PGE layer	56.1	21300.0	2594.0	2255.6	11875.1	13735.0	27340.0	308.0	1000.0	1170.0	167.0	757.0	1247.9	25.3	0.4	0.1	0.2
Zunyi 14	5.6	Black shale	2.2	43000.0	98.3	97.2	237.9	539.0	1050.0	25.2	17.8	2590.0	73.5	384.0	430.9	60.7	1.1	0.1	0.2
Sancha 1	0.1	Phosphorite layer	0.6	4100.0	49.3	80.9	129.8	76.8	67800.0	2.8	12.5	640.0	178.1	306.0	28.9	0.2	8.2	0.5	0.6
Sancha 2	0.3	Ni-Mo-PGE layer – rich in phosphorites	29.4	9300.0	3641.8	564.6	10223.0	5941.0	8630.0	59.8	660.4	570.0	529.7	1201.0	362.7	16.7	7.6	0.3	0.4
Sancha 3	0.3	Ni-Mo-PGE layer	9.0	29600.0	1820.9	525.0	4000.0	5015.9	26720.0	49.6	761.2	1730.0	577.6	6080.0	90.7	14.7	7.1	0.3	0.3
Sancha 4	0.5	Black shale	0.8	24700.0	33.2	30.5	101.4	104.7	593.0	20.3	7.0	1554.0	39.3	612.0	268.0	51.3	7.5	0.3	0.5
Sancha 5	0.6	Black shale	0.7	42012.0	35.4	38.5	168.9	197.9	375.0	22.3	11.2	2177.0	40.1	1045.0	136.0	70.6	9.5	0.7	0.4
Sancha 6	0.7	Black shale	0.8	37100.0	28.3	57.7	143.0	200.0	290.0	18.8	9.6	2300.0	47.4	1032.0	184.4	75.5	4.2	0.4	0.4
Sancha 7	0.8	Black shale	1.1	50293.0	43.0	48.7	123.7	112.6	281.0	31.1	10.1	2506.0	64.7	393.0	127.0	80.3	10.1	0.7	0.7
Sancha 8	1.1	Black shale	1.0	49300.0	26.0	89.1	122.1	187.8	360.0	22.1	10.8	2690.0	55.5	794.0	93.4	80.9	13.6	0.7	0.4
Sancha 9	1.3	Black shale	1.3	60356.0	43.6	65.6	186.1	165.9	1199.0	25.5	14.2	2620.0	74.0	699.0	90.0	84.3	10.8	0.8	0.3
Sancha 10	1.5	Black shale	1.3	47900.0	41.6	37.8	93.4	175.4	160.0	22.8	10.6	2860.0	25.6	280.0	275.8	83.1	8.4	0.5	0.7
Sancha 11	1.6	Black shale	1.2	55117.0	47.3	42.0	92.3	194.3	286.0	25.2	9.7	2636.0	32.6	273.0	299.0	80.6	9.2	0.4	0.2
Sancha 12	1.7	Black shale	1.1	45900.0	37.2	92.3	114.8	140.3	550.0	22.2	10.4	2690.0	62.6	241.0	312.7	79.6	8.5	0.8	0.7
Sancha 13	2.1	Black shale	1.8	52262.0	73.6	62.8	115.4	104.8	510.0	32.5	13.3	2538.0	60.6	248.0	133.0	81.8	6.9	0.2	0.3
Sancha 14	2.3	Black shale	2.4	48200.0	56.5	124.9	135.2	98.5	900.0	28.8	17.7	2830.0	77.5	325.0	71.4	83.8	7.7	0.3	0.4
Sancha 15	2.5	Black shale	2.3	41469.0	71.0	73.5	143.3	214.8	534.0	31.6	24.7	2087.0	61.5	585.0	288.0	66.8	8.2	0.4	0.3
Jinsha 1	17.00	Dolostone	0.1	417.0	0.5	8.2	0.2	0.7	136.0	1.6		24.0	0.4	2.0	3.0	1.5	0.1	0.1	0.2
Jinsha 2	45.00	Black shale	0.7	84944.0	11.4	16.5	17.1	14.4	398.0	34.7	0.6	4626.0	16.7	212.0	55.0	126.7	2.5	0.2	0.2
Jinsha 3	59.00	Black shale	14.2	4444.0	116.2	57.2	133.9	27.3	78625.0	27.6	86.2	209.0	194.1	1781.0	82.0	4.1	6.4	0.4	0.1
Jinsha 4	62.00	Black shale	0.2	95875.0	3.5	10.1	4.9	44.9	880.0	8.2	0.6	4618.0	7.7	322.0	59.0	134.5	1.2	0.3	3.2
Jinsha 5	66.00	Siltstone	0.1	89175.0	4.6	52.0	1.0	58.7	732.0	20.8		4762.0	4.4	180.0	112.0	115.6	0.2	0.1	0.6
Jinsha 6	76.00	Siltstone	0.1	61133.0	1.8	84.0	1.6	44.7	1226.0	4.4		3797.0	2.5	101.0	140.0	78.7	0.3	0.1	0.2
Jinsha 7	86.00	Limestone	0.1	49364.0	8.1	141.5	1.3	38.3	1882.0	6.7		2209.0	3.2	93.0	348.0	58.4	0.2	0.1	0.6
Jinsha 8	97.00	Limestone	0.2	8956.0	9.9	20.6	2.3	5.9	88.0	77.7		560.0	1.1	12.0	73.0	15.0	0.3	0.1	0.2
Nick		Mineralised layer	7.8	9996.0	3313.8	379.6	3192.4	60371.0	937.0	112.3	2160.8	450.0	67.0	543.0	9733.0	19.1			

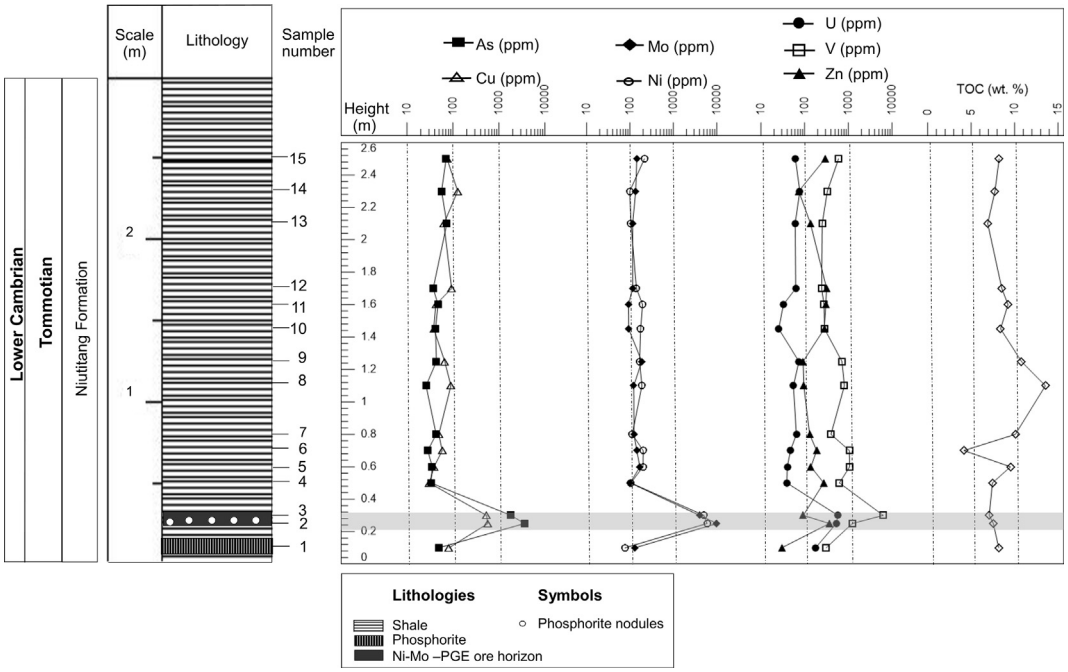

Fig. 5. Sedimentological log and As, Cu, Mo, Ni, U, V and Zn concentrations from the Sancha samples. The grey bar indicates the ore horizon.

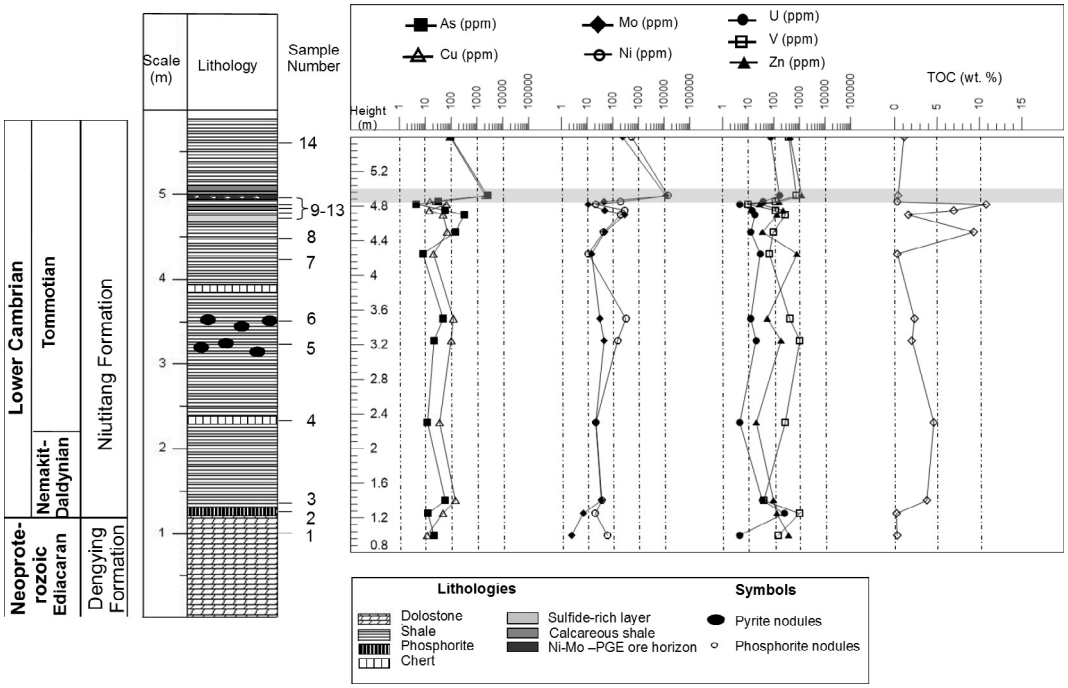

Fig. 6. Sedimentological log and As, Cu, Mo, Ni, U, V and Zn concentrations from the Zunyi samples. The grey bar indicates the ore horizon.

5. Discussion

5.1. Redox conditions in Niutitang shales and the Nick deposit

A characteristic of both the Niutitang and Nick polymetallic sulphide layers is concentration and fine microlayering of redox-sensitive elements. Both the REE (Fig. 9) and PGE (Fig. 8) distribution patterns of Zunyi and Sancha present strong similarities with seawater patterns, although concentrations at both sites are much more enriched than seawater. These similarities, further discussed in Section 5.3, imply a likely metal source from seawater.

Under oxic conditions, V occurs as V^{5+} in vanadate oxyanions. Under suboxic conditions, V is present as V^{4+} and forms the vanadyl ion (VO^{2+}), forming hydroxyl species $VO(OH)_3^-$ or the insoluble hydroxide $VO(OH)_2$. In marine environments, the V^{4+} ionic species can form organo-metallic complexes or can be trapped to sediments by surface adsorption mechanisms. Under euxinic conditions, V is further reduced to V^{3+}, which can be incorporated into metallo-porphyrins or precipitated as solid oxide V_2O_3 or a hydroxide $V(OH)_3$ phase (Algeo and Maynard, 2004; Scott et al., 2017; Tribovillard et al., 2006; Wanty and Goldhaber, 1992). V is typically enriched in sediments deposited under reducing conditions. Cr is commonly incorporated within the detrital clastic fraction of sediment where it may substitute for Al within clays (Patterson et al., 1986). V/Cr ratio has been used as a

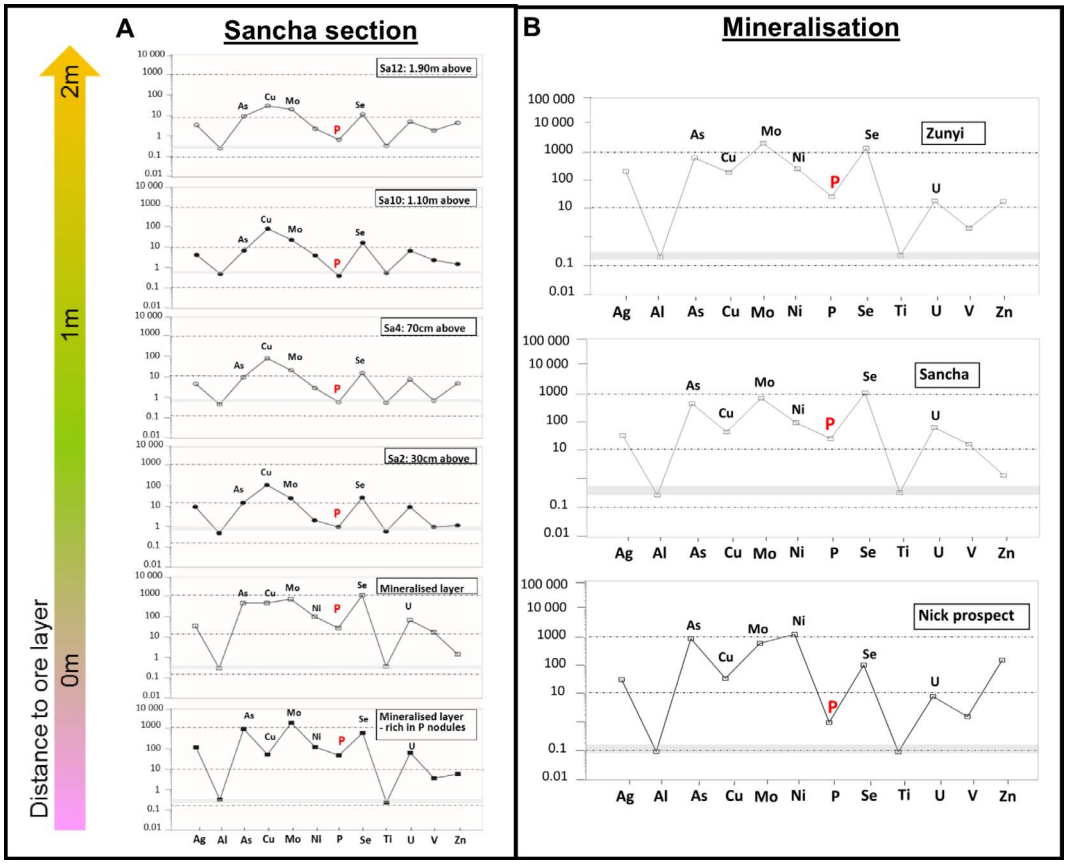

Fig. 7. Enrichment factors in Ag, Al, As, Cu, Mo, Ni, P, Se, Ti, U, V, Zn normalised to the concentrations of one barren shale sample from Jinsha. A) Sancha section (ore body to 2 m away). B) Comparison between enrichment factors in Zunyi, Sancha and the Nick deposit.

Table 2
PGE concentrations (in ppb) from Zunyi, Sancha and the Nick deposit.

Sample	Au	Ir	Os	Pd	Pt	Re
Zunyi mineralised layer	65.0	3.0	88.1	203.0	417.1	31.5
Sancha mineralised layer	147.1	3.5	39.5	290.5	287.2	10.3
Nick mineralised layer	95.8	3.5	24.3	216.5	182.9	4.4

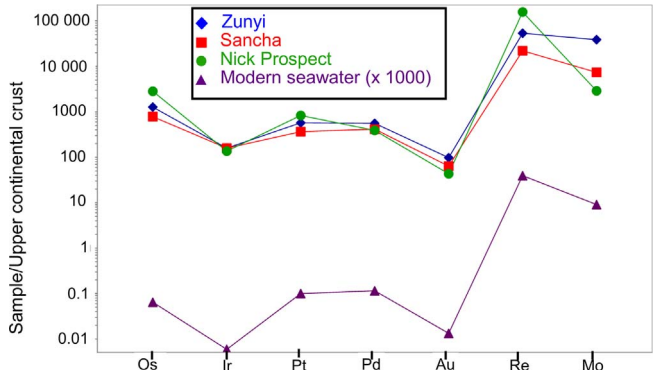

Fig. 8. PGE distribution patterns for Zunyi, Sancha, the Nick deposit and modern seawater (Nozaki, 1997).

paleoredox proxy with high values indicative of anoxic conditions and low values suggesting suboxic to oxic conditions (Jones and Manning, 1994). Formation of organo-metallic complexes between Ni and organic matter can increase the rate of scavenging in the water column and consequently, Ni accumulation in sediments (Piper and Perkins, 2004). Under oxic conditions, Ni can be present as soluble cations Ni^{2+}, $NiCl^{+}$ ions or Ni carbonates $NiCO_3$ (Calvert and Pedersen, 1993). Under euxinic conditions, however, Ni tends to precipitate with sulphide and can be incorporated as insoluble NiS into pyrite (Morse and Luther, 1999). Ni/Co ratio has been used as a paleoredox index with high values reflecting reducing conditions.

Ratios of trace elements have been commonly used to highlight palaeo-redox conditions prevailing during shale deposition (e.g. Hatch and Leventhal, 1992; Jones and Manning, 1994). V/Cr and Ni/Co commonly show a decrease in value with increasing oxygen concentrations in the water column (Xu et al., 2012). Fig. 13 presents the distribution of V/Cr versus Ni/Co and Mo concentrations versus Ni/Co. These plots indicate that both mineralised layers in Zunyi and Sancha as well as the Nick deposit were deposited under euxinic conditions. Samples collected above the mineralisation and below the mineralisation in Zunyi were also deposited under euxinic conditions. Although one sample collected below mineralisation in Zunyi plotted as “dysoxic” (0.2–2 mL/L of oxygen) in the V/Cr versus Ni/Co plot, it plotted as euxinic in the other plots, suggesting that this sample was likely deposited under euxinic conditions. However, the sample from barren shale in Jinsha (used as a reference for calculating the enrichment factors in Zunyi, Sancha and the Nick deposit) appeared to be deposited under dysoxic (0.2–2 mL/L of oxygen) to suboxic conditions (Null – Null.2 mL/L of oxygen) (Tyson and Pearson, 1991).

Plots of Mo versus U enrichment factors (EF) were also used to assess palaeo-redox conditions. Co-variations of Mo and U EF have been successfully applied to assess prevailing redox conditions in several sedimentary systems (Algeo and Tribovillard, 2009; Tribovillard et al., 2012). Under reducing conditions, U is scavenged at the sediment-water interface. The activity of sulphate-reducing bacteria promotes the uptake of insoluble U(IV) by organic matter leading to the formation of organometallic complexes. Mo is also taken up at the sediment-water

Table 3
REE + Y concentrations (in ppm) from Zunyi, Sancha and the Nick deposit.

Sample	Depth (m)	Lithology	Ce	Dy	Er	Eu	Gd	Ho	La	Lu	Nd	Sm	Tb	Tm	Y	Yb
Zunyi 1	1	Dolostone	5.97	0.9	0.61	0.19	0.95	0.2	5.58	0.08	4.04	0.81	0.13	0.08	9.32	0.53
Zunyi 2	1.3	Phosphorite layer	204.52	46.7	28.0	11.2	57.0	11.4	244.30	2.2	225.2	47.6	8.1	3.7	513.9	16.4
Zunyi 3	1.4	Black shale	110.00	16.3	9.5	0.9	16.9	3.7	42.30	1.3	69.4	18.9	4.2	1.6	67.7	8.6
Zunyi 4	2.3	Chert	5.36	0.7	0.5	0.1	0.8	0.2	3.70	n.d.	3.2	0.7	n.d.	n.d.	6.5	0.8
Zunyi 5	3.3	Black shale rich in pyrite nodules	43.56	3.6	2.2	1.1	4.3	0.8	20.50	0.4	20.5	4.1	0.75	0.3	21.4	2.3
Zunyi 6	3.5	Black shale rich in pyrite nodules	11.84	1.8	1.3	0.5	1.9	0.5	4.40	0.2	8.1	1.8	0.2	0.2	13.8	1.3
Zunyi 7	4.3	Black shale	52.94	6.8	4.2	2.5	8.8	1.6	47.60	0.3	41.0	8.1	1.1	0.5	80.3	2.6
Zunyi 8	4.5	Black shale	7.73	5.1	2.5	1.3	6.2	1.1	2.60	0.3	16.6	5.6	0.9	0.4	31.6	2.1
Zunyi 9	4.7	Sulfide-rich layer	42.65	1.7	1.3	0.4	1.8	0.4	20.00	0.3	18.7	2.7	0.1	0.2	10.2	1.6
Zunyi 10	4.8	Black shale	10.68	1.7	1.2	0.3	1.8	0.5	5.80	0.2	6.4	1.6	0.1	0.2	13.9	1.3
Zunyi 11	4.8	Calcareous shale	14.29	1.13	0.76	2.56	1.19	0.27	10.94	0.08	5.06	0.9	0.17	0.09	13.63	0.53
Zunyi 12	4.9	Black shale	12.44	1.09	0.78	0.67	1	0.25	10.41	0.1	5.2	0.93	0.16	0.12	12.1	0.73
Zunyi 13	4.9	Ni-Mo-PGE layer	61.49	6.1	3.4	2.7	7.0	1.4	34.20	0.3	35.0	6.5	0.9	0.5	60.0	2.2
Zunyi 14	5.6	Black shale	43.59	3.6	2.1	0.9	4.0	0.9	23.10	0.3	22.7	4.2	0.4	0.3	27.4	2.1
Sancha 1	0.1	Phosphorite layer	39.14	4.03	2.82	0.83	4.13	0.93	19.73	0.37	17.61	3.75	0.63	0.37	31.38	2.47
Sancha 2	0.3	Ni-Mo-PGE layer – rich in phosphorites	49.94	4.6	2.8	1.3	5.6	1.1	18.10	0.4	26.6	6.2	0.7	0.5	29.1	2.8
Sancha 3	0.3	Ni-Mo-PGE layer	51.89	3.77	2.54	0.83	3.81	0.85	26.31	0.37	20.68	3.96	0.59	0.37	24.87	2.48
Sancha 4	0.5	Black shale	41.34	4.0	2.8	0.9	3.9	1.1	17.20	0.5	17.6	3.2	0.5	0.5	33.7	3.0
Sancha 5	0.6	Black shale	49.79	3.73	2.67	0.81	3.8	0.85	26.31	0.39	19.62	3.64	0.59	0.38	29.66	2.52
Sancha 6	0.7	Black shale	41.34	3.6	2.7	0.8	3.5	1.0	18.20	0.4	17.6	3.1	0.4	0.4	36.2	2.4
Sancha 7	0.8	Black shale	74.85	5.63	3.21	1.56	6.99	1.13	34.92	0.41	35.93	7.5	0.97	0.44	31.24	2.88
Sancha 8	1.1	Black shale	25.19	2.8	2.0	0.7	3.0	0.7	10.20	0.3	13.5	2.4	0.3	0.4	17.8	2.0
Sancha 9	1.3	Black shale	44.97	3.04	2.11	0.71	3	0.67	24.57	0.32	17.5	3.13	0.47	0.31	19.15	2.18
Sancha 10	1.5	Black shale	35.97	2.2	1.8	0.5	1.9	0.6	17.10	0.3	13.7	2.3	0.2	0.3	20.0	1.9
Sancha 11	1.6	Black shale	38.98	2.23	1.64	0.49	2.17	0.51	21.12	0.27	15.63	2.63	0.32	0.25	16.31	1.8
Sancha 12	1.7	Black shale	31.67	1.92	1.36	0.47	1.93	0.43	17.08	0.21	11.95	2.13	0.28	0.19	13.29	1.34
Sancha 13	2.1	Black shale	215.39	46.1	26.5	9.6	54.2	11.0	171.90	2.6	211.9	44.8	7.8	3.5	477.0	1731.0
Sancha 14	2.3	Black shale	192.36	34.2	18.8	7.8	41.3	7.9	89.00	1.5	195.8	39.3	5.8	2.4	347.3	10.5
Sancha 15	2.5	Black shale	94.80	27.0	20.1	5.5	27.7	7.6	106.10	2.6	96.4	20.2	4.5	3.0	309.0	16.4
Jinsha 1	17.00	Dolostone	1.01	0.17	0.1	0.04	0.2	0.04	0.99	0.01	0.83	0.16	0.03	0.01	1.88	0.07
Jinsha 2	45.00	Black shale	71.03	3.38	2.26	0.96	3.48	0.7	38.1	0.39	28.32	4.91	0.53	0.35	17.34	2.46
Jinsha 3	59.00	Black shale	49.15	30.66	20.06	7.39	35.83	7.08	58.2	1.75	102.6	26.61	4.84	2.37	330.88	13.43
Jinsha 4	62.00	Black shale	56.21	3.76	2.66	0.91	3.98	0.85	30.49	0.39	24.96	4.65	0.59	0.39	22.74	2.75
Jinsha 5	66.00	Siltstone	87.64	6.35	3.63	1.87	8.11	1.25	45.47	0.49	43.12	8.79	1.12	0.49	33.05	3.35
Jinsha 6	76.00	Siltstone	57.57	4.79	3.02	1.43	5.97	0.95	26.58	0.32	27.98	6.39	0.84	0.36	23.72	2.42
Jinsha 7	86.00	Limestone	34.36	4.3	2.24	1.13	5.37	0.8	14.99	0.29	20.12	5.26	0.75	0.31	26.14	1.92
Jinsha 8	97.00	Limestone	15.39	1.08	0.61	0.27	1.18	0.21	8.2	0.08	6.85	1.31	0.18	0.09	5.91	0.52
Nick		Mineralised layer	71.41	13.63	7.81	3.36	16.68	2.81	71	0.72	87.45	17.33	2.29	0.94	107.94	5.38

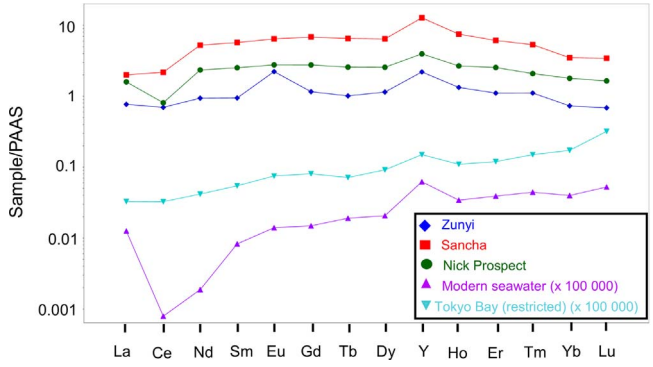

Fig. 9. REE and Y distribution patterns normalised to PAAS (Post-Archean Australian shales) for Zunyi, Sancha, the Nick deposit, modern seawater (Nozaki, 1997) and the Tokyo Bay (restricted environment; Nozaki and Zhang; 1995).

interface, however, this mechanism requires the formation of thiomolybdates driven by free H_2S. Therefore, a greater uptake of U in comparison to Mo occurs under sub-oxic conditions (Algeo and Tribovillard, 2009; Wagner et al., 2017). EF in Mo and U can therefore be used as a proxy for characterising palaeo-environmental conditions.

Mo and U EF are calculated as follows:

$$X_{EF} = [(X/Al)_{sample}/(X/Al)_{PAAS}]$$

with X and Al representing the weight percent concentrations of elements X and Al, respectively. Samples were normalised using the post-Archean average shale (PAAS) compositions of Taylor and McLennan (1985).

$(Mo/U)_{EF}$ ratios of ~0.1–0.3 × SW are characteristic of suboxic conditions, $(Mo/U)_{EF}$ ratios of 0.3–1 × SW indicate anoxic conditions while $(Mo/U)_{EF}$ ratios of 1–3 × SW suggest euxinic conditions in open marine settings. Strong enrichment in Mo in comparison to U though, commonly reveals the mechanism of metaloxyhydroxide particulate shuttle that promotes the export of aqueous Mo to the sediment (with limited impact on aqueous U). Under such conditions, $(Mo/U)_{EF}$ ratios exceed the seawater ratio (3–10 × SW) and present a "particulate shuttle" trend, different from the unrestricted marine trend (Algeo and Tribovillard, 2009).

In the present study, the distribution of the samples presents an open marine trend. All samples including the mineralised horizons in Zunyi and Sancha and the samples above and below mineralisation present $(Mo/U)_{EF}$ values characteristic of euxinic conditions (Fig. 13). This plot also shows that the Nick deposit was formed under euxinic conditions. However, the sample from the barren shale in Jinsha shows values characteristic of suboxic conditions.

5.2. Phosphorite nodules in China shales

Abundant phosphorite nodules and fragments were detected in samples from both Zunyi and Sancha (Figs. 11 and 12). Additional phosphorite nodules are found at the transition between the Dengying Formation and the Niutitang Formation. These economic-grade phosphorites are being mined at different sites (e.g. Zhijin phosphorite deposit, near the Maluhe polymetallic sulphide ore deposit, Guizhou

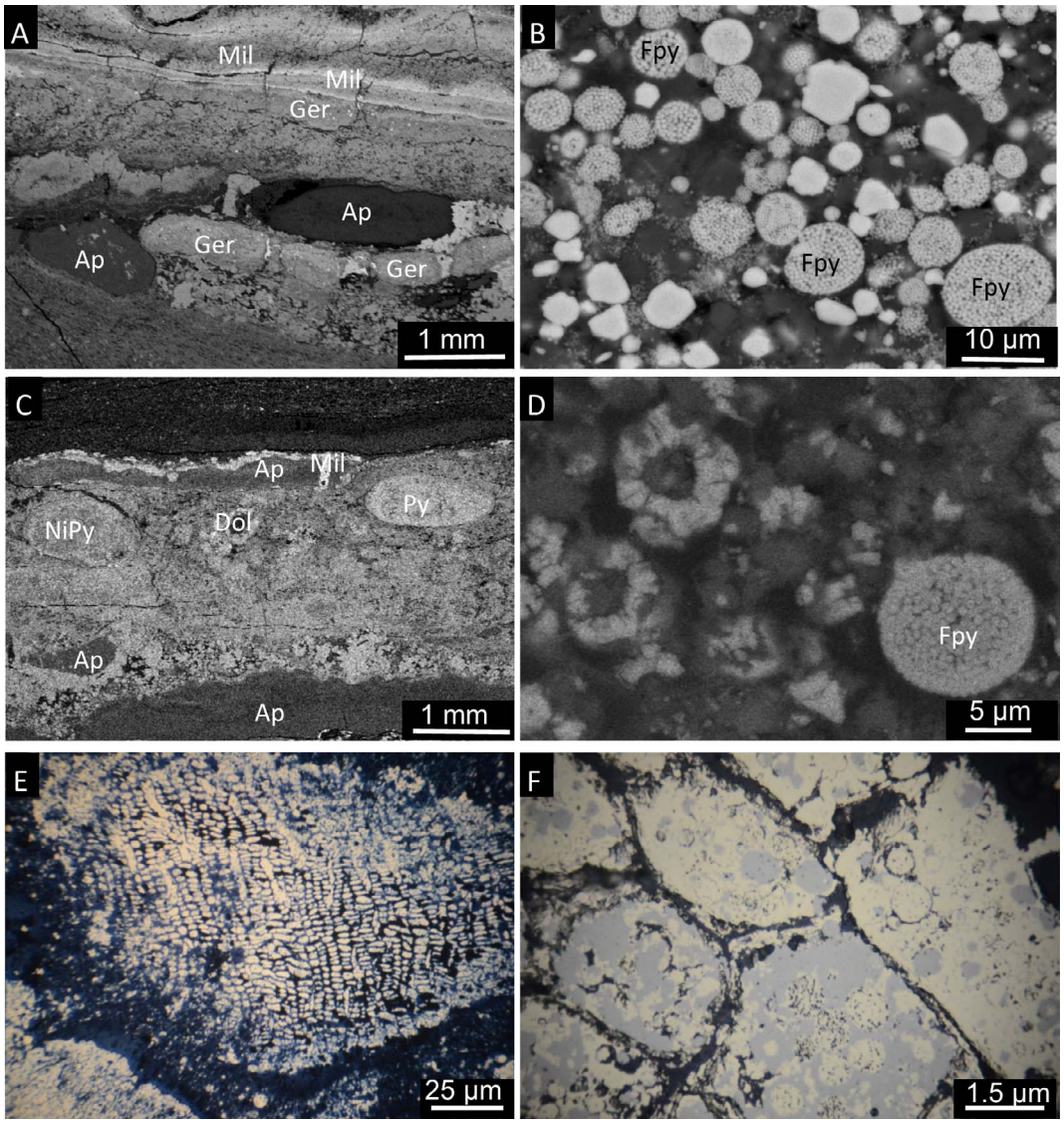

Fig. 10. Photomicrographs of A) the mineralised layer in Zunyi. B) Framboidal pyrites detected in the mineralised layer in Zunyi. C) Photomicrographs of the mineralised layer in Sancha. D) Framboidal pyrites detected in the mineralised layer in Sancha. E) Wood material in the Nick deposit F) Composite cells from the wood material present in the Nick deposit. Ap: Apatite. Dol: Dolomite. Ger: Gersdorffite. Fpy: Framboidal pyrite. Mil: Millerite. Nipy: Nickeliferous pyrite. Py: Pyrite.

Province). Worldwide, modern phosphorite deposits are consistently found at low latitudes, due to their dependence on warm nutrient-rich waters to form the organic-rich sediments from which phosphates precipitates. Sediment accumulation rates between 2×10^5 and 1×10^6 years per meter have been estimated for economic-grade phosphorites (Slansky, 1986). Therefore, the occurrence of the phosphorites in the lower part of the formation suggests deposition in a shallow water, low energy environment with a very low rate of supply of clastic material. A high salinity environment has been also suggested for the formation of the phosphorites (Pašava et al., 2008).

A recent study by Reinhard et al. (2017) showed a compilation of P abundances in the rock record over the past 3.5 billion years, highlighting the evolution of P cycle through time. The authors reported low authigenic P burial in shallow marine environments until about 800 to 700 million years ago, related to the presence of anoxic, iron-rich conditions. Iron-rich redox conditions would have promoted the effective removal of bioavailable P from surface waters via the formation of ferrous phosphate phases and carbonated/sulphated green rust. The abrupt increase in P content in the rock record could reflect a drastic change in the P cycle between 800 and 635 Ma, suggesting that P availability suddenly increased in the Cambrian oceans (Reinhard et al., 2017).

Phosphorite nodule formation can be promoted abiogenically and biogenically. Under anoxic conditions, the rapid reduction of iron(III) oxyhydroxides – P complexes deriving from continental weathering to dissolved Fe(II) results in the release of P into the porewater environment (Van Cappellen and Berner, 1988). Nonetheless, recent studies on continental margin sediments highlighted that organic matter is the most significant shuttle of reactive P to the seafloor (Filippelli, 2008). Organic P can be released via direct oxidation in the water column, at the sediment-water interface or after burial. When organic P gets released underneath the sediment-water interface, P concentrations in the pore water can be high enough to induce the precipitation of phosphorite that gets permanently stored in the sediments and becomes resistant to further release.

In shallow waters, microbial activity can also strongly promote the precipitation of phosphorite nodules. Microbial activity can lead to rapid redox disequilibrium and microbial mats, for instance, can favour phosphogenesis through the production of localised dysaerobic microenvironments, further promoting rapid phosphate mineralisation (Pagès et al., 2015, 2014a). Microbial mats also tend to accumulate calcium carbonate required for apatite precipitation (Wilby et al., 1996)

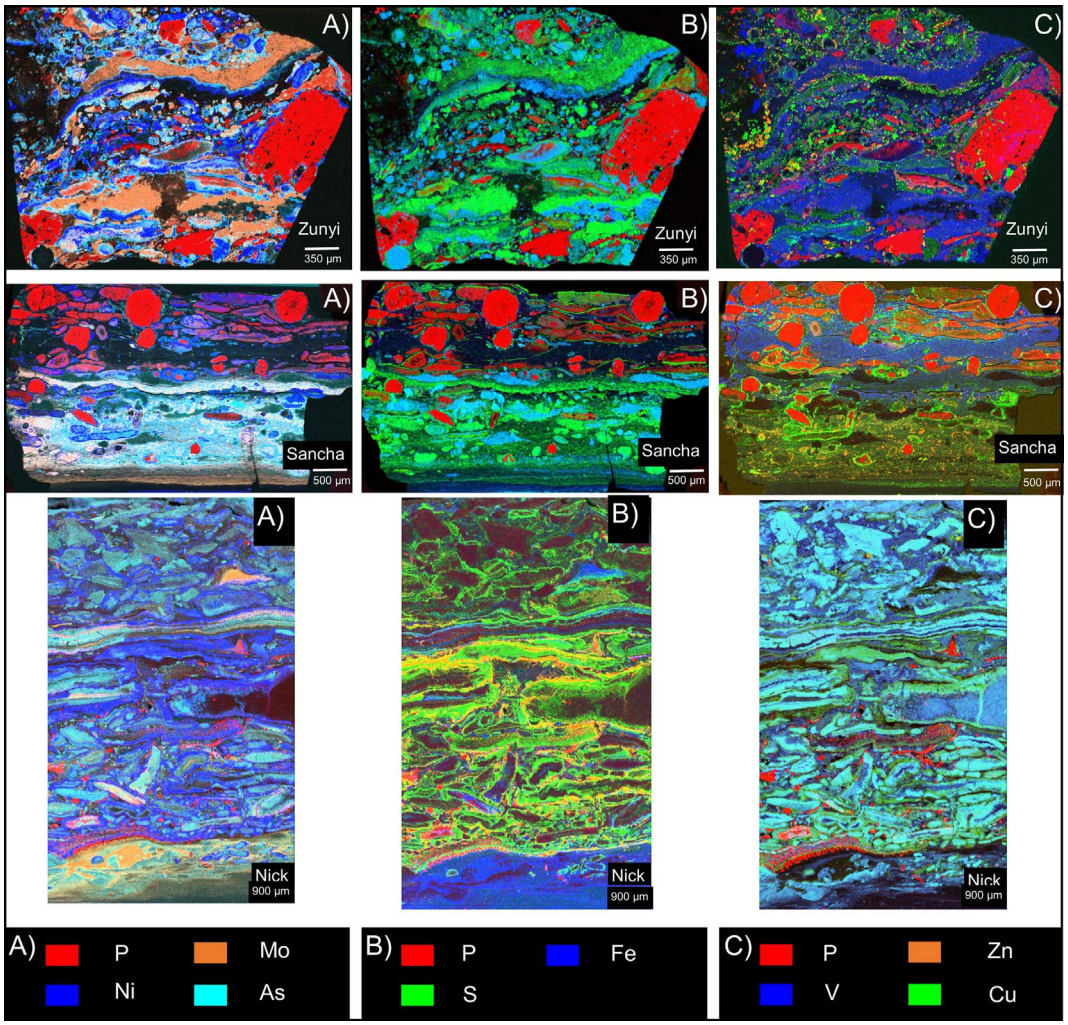

Fig. 11. Microbeam XRF elemental mapping of samples from Zunyi (top row), Sancha (middle row) and the Nick deposit (bottom row). A) Distribution of P, Ni, Mo and As. B) Distribution of P, Fe and S. C) Distribution of P, V, Zn and Cu. Abundant phosphorite fragments and brecciated textures are present in the Zunyi and Sancha samples. Fine laminations of P, Ni, As, Mo and S and a high abundance of Ni and As-rich sulphide clasts are observed in the Zunyi sample. In the Sancha sample, one part of the sample contains abundant As and Cu while the other part contains abundant phosphorite nodules associated with V-rich clay and Ni-rich lenses. The Nick deposit sample does not show phosphorite nodules and presents elongated lenses of pyrite and As-rich phase surrounded by fine laminations of Ni.

via bacterial extracellular polymeric substances (EPS) production and alkalinity production, and have the ability to create a barrier to outward diffusion of dissolved phosphate. In the Peru margin phosphorites, the main source of phosphate is derived from the microbially-driven release of P from phospholipids and other phosphate compounds originating from plankton debris (Froelich et al., 1988). Therefore, effective Fe-P cycling, decomposition of bacterially mediated P and active microbial activity could have led to enrichment in porewater P and favourable redox conditions for apatite precipitation. The early diagenesis of phosphorite nodules favours outstanding preservation of original depositional materials such as fossils, coprolites and other sedimentological information. As they lithify, sedimentary phosphorite nodules tend to incorporate REE (e.g. Kidder et al., 2003). Furthermore, experiments undertaken to assess the capacity of hydroxyapatite to reduce the solubility of metals in contaminated sediments successfully showed that Ni and U, for instance, were being sequestered by hydroxyapatite amendment (Seaman et al., 2001). The high abundance of phosphorite nodules in samples from both Zunyi and Sancha that are located hundreds of km apart strongly suggests that similar environmental conditions must have prevailed in different locations of the platform. It is likely that these platform areas acted as traps for continental particulate matter derived, promoting a decrease in pelagic sedimentation rates and leading to a sediment starved basin. The presence of microbial activity would have further promoted the precipitation of phosphorite nodules in this euxinic basin.

5.3. Comparison between Zunyi and Sancha

Plots of trace element ratios highlight that the samples from the mineralised layer in both Zunyi and Sancha as well as the host shales were deposited under euxinic conditions (Fig. 13). In addition, similar concentrations in trace elements were detected at both sites. The comparison of enrichment factors in Ag, Al, As, Cu, Mo, Ni, P, Se, Ti, U, V and Zn between Sancha and Zunyi shows strikingly similar patterns of enrichment factors with As, Cu, Mo, Ni, Se being the most enriched elements at both sites (Fig. 7), even though these two sites are located more than 600 km apart. High maturity of organic matter was detected at both sites, with very low S1 values (0–1) and no detectable S2 values from Rock Eval pyrolysis. Samples from the mineralised horizon in Zunyi and Sancha both show a very similar distribution of PGE and REE (Figs. 8 and 9). P is also enriched at both sites and abundant phosphorite nodules and fragments were detected at both locations from the XRF maps (Figs. 11 and 12). Finally, samples from both study sites also present a strong heterogeneity in elemental distributions (Figs. 11 and 12), likely reflecting the rapid changes at µm-scale in redox conditions.

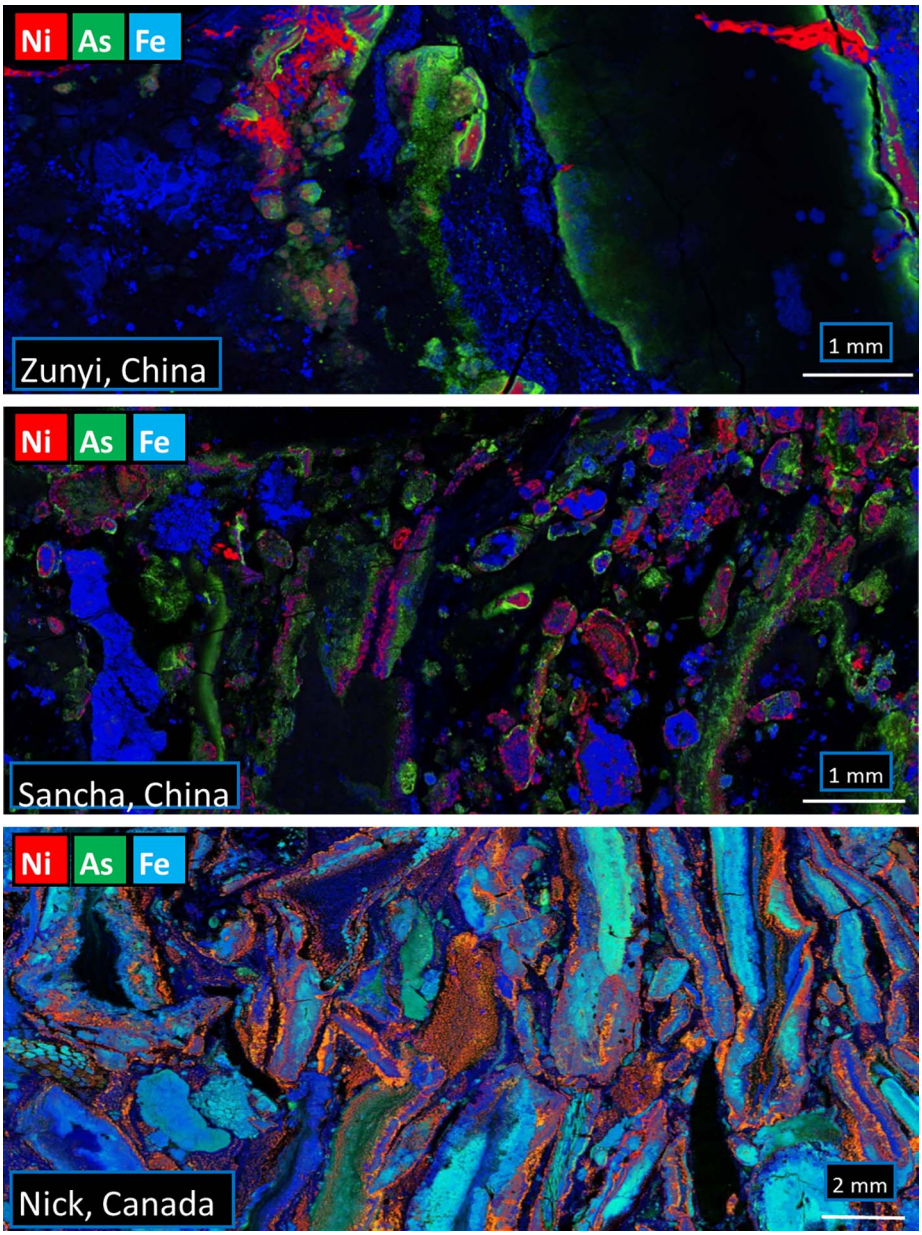

Fig. 12. Synchrotron-based XRF elemental mapping of samples showing Ni, As, Se distributions in Zunyi (top row), Sancha (middle row) and the Nick deposit (bottom row).

5.4. Metal enrichment in Zunyi and Sancha

There is long-standing debate about the origin of this mineralised layer. Emsbo et al. (2005) proposed a model involving a submarine petroleum discharge leading to the formation of a surface oil slick and metal-rich tar balls progressively sinking to the bottom of the basin. Other studies have proposed either a hydrothermal origin (e.g. Li and Gao, 1996; Lott et al., 1999; Murowchick et al., 1994) or a seawater scavenging source (e.g. Lehmann et al., 2016; Mao et al., 2002).

In the present study, the plots of trace element ratios point towards a euxinic depositional environment for Zunyi and Sancha (Fig. 13). In addition, the strong resemblance between PGE distribution in Sancha and Zunyi suggests a similar source of PGE (Fig. 8). PGE distribution in both Niutitang sites also show remarkably similar patterns with seawater PGE distribution pattern, although at both sites, PGE concentrations are about 4 orders of magnitude more enriched than seawater. Lehmann et al. (2016) reported that plots of Re versus Os concentrations from Cambrian China shales (Zunyi) were consistent with the trend of the reference black shale and were more enriched in both elements by about one order of magnitude. Previous studies of Os isotopic data suggest that Re and PGE enrichment of the mineralised horizons in the Niutitang shales probably occurred near the time of sediment deposition or during early diagenesis (Horan et al., 1994). The near 1: 1: 1 Au/Pd/Pt ratios of the Cambrian South China shales, also reported by Mao et al. (2002) and Lehmann et al. (2003), do not coincide with ratios found in Pt- or Pd-enriched hydrothermal deposits and tend to support a seawater origin, with metals being scavenged from the overlying water column. In addition, the relatively low Ir concentrations and high Re concentrations observed at both Chinese sites do not support an extra-terrestrial source of PGE, as previously proposed by Goodfellow et al. (2010).

The REE patterns of Sancha and Zunyi present strong similarities with REE patterns from the Tokyo Bay (restricted environment), although the REE in Zunyi and Sancha are 7 to 8 times more enriched than in seawater samples (Fig. 9). Both Zunyi and Sancha samples present a positive Y anomaly, also detected for the modern seawater and the Tokyo Bay. The light-REE, in particular La and Ce, are depleted in the South China samples and the seawater samples. While the

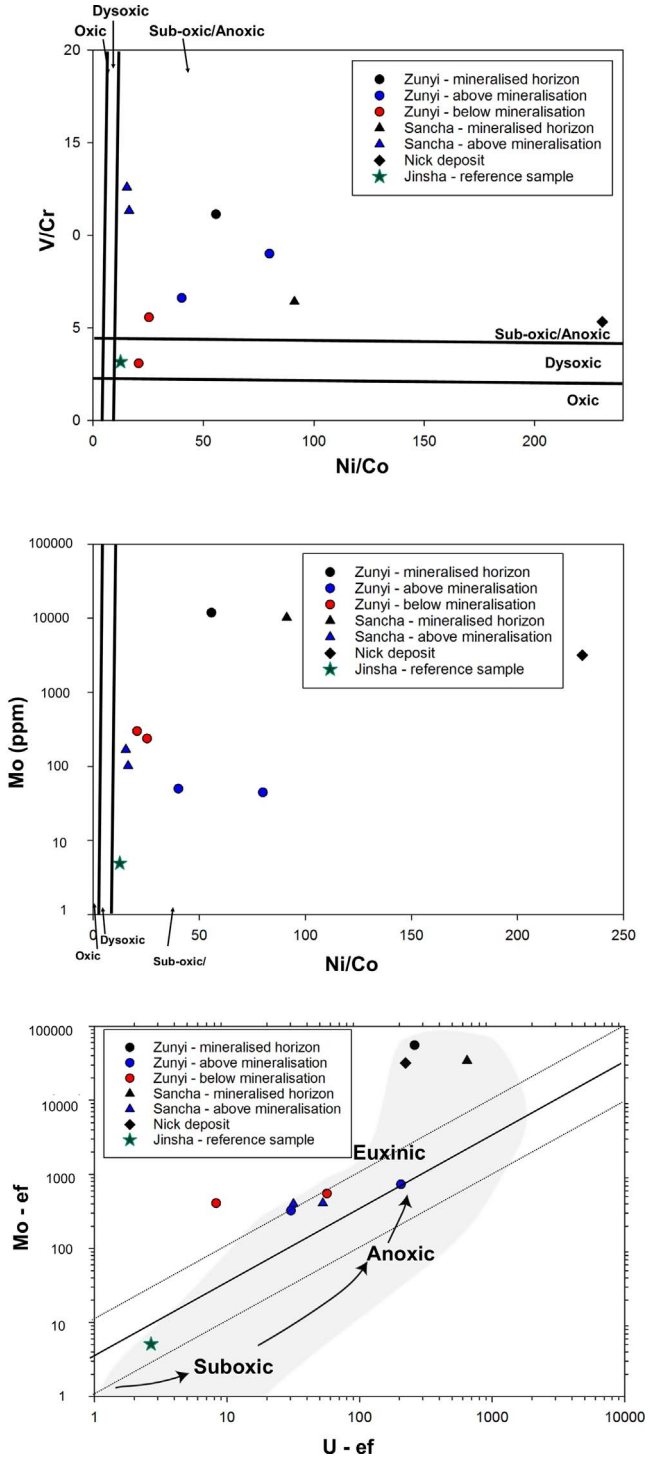

Fig. 13. Cross-plots of trace element ratios used as palaeo-redox proxies. A: V/Cr vs. Ni/Co, B: Mo vs. Ni/Co, C: S vs TOC, D: U-enrichment factor (EF) versus Mo-EF. Thresholds for different redox environments based on Ni/Co and V/Cr from Jones and Manning (1994). The oxic field corresponds to oxygen concentrations > 2 mL/L, dysoxic between 0.2 and 2 mL/L, suboxic between 0 and 0.2 mL/L (Tyson and Pearson, 1991). U-EF versus Mo-EF based on Algeo and Tribovillard (2009). The lines represent multiples (0.3, 1, and 3) of the Mo:U ratio of modern-day seawater:molar ratios of ~7.9 for the Atlantic and ~7.5 for the Pacific converted to an average weight ratio of 3.1 or comparison with sediment Mo:U weight ratios (Tribovillard et al., 2012).

modern seawater presents a strong negative Ce anomaly, the Tokyo Bay sample presents a less pronounced negative Ce anomaly, similar to the ones observed in Zunyi and Sancha. The mineralised layer in Zunyi, however, presents a slightly positive Eu anomaly. Positive Eu anomalies can be caused by weathering processes or hydrothermal overprint related to exposure to acidic, reducing hydrothermal fluids with temperatures > 250 °C (Bau, 1991). This is inconsistent with the study from Kříbek et al. (2007) highlighting that the mineralised layer in Zunyi had not been exposed to fluids hotter than 200 °C. Positive Eu anomalies can also develop during deposition and digenesis under reducing conditions (e.g., MacRae et al., 1992; Martinez-Ruiz et al., 1999). In addition, a recent experimental study observed Eu(II) species in reduced aqueous solutions at ambient temperature, with its stability increasing as temperature rises (Liu et al., 2017). Thermodynamic calculations predicted that, under reducing and slightly alkaline conditions, Eu^{2+} can also reach its field of stability, promoting a positive Eu anomaly (Sverjensky, 1984). As previously suggested by Xu et al. (2013), it is therefore possible that the slight positive Eu anomaly observed in Zunyi could reflect the activity of sulphate-reducing bacteria promoting alkaline conditions, as in the modern Black Sea.

Finally, Mo was extremely enriched at both sites (3 orders of magnitude more enriched than in Jinsha's barren shales) (Fig. 7). Hydrothermal fluids in oceanic settings are typically not enriched in Mo, relative to seawater, further discarding a hydrothermal origin for these mineralised layers (Scott et al., 2014).

Therefore, the strong similarity in metal concentrations, enrichment patterns, including PGE and REE, and metal distributions over hundreds of km tend to favour a common mineralisation style at both sites and suggest a possible source from seawater.

5.5. Similarity and differences in South China shales and the Nick deposit

The comparison of different characteristics from Zunyi, Sancha and the Nick deposit is summarised in Table 4. Samples from the Niutitang shales and the Nick deposit contain diverse minerals and similarly complex microstructures suggesting a degree of similarity in mineralisation processes. Nonetheless, the Niutitang samples present more brecciated textures along with fine metal laminations, while the Nick deposit sample shows sulphide lenses surrounded by metal laminations (e.g. Zn and Cu) (Fig. 11). In addition, although fluorapatite was detected in the Nick deposit, the abundance of phosphorite nodules and fragments is much greater in the Niutitang samples. The samples from Niutitang present a greater diversity of minerals and contain arsenopyrite, chalcopyrite, covellite, vaesite, gersdorffite, barite, bravoite, sulvanite, pentlandite, tennantite, tiemannite, violate and coffinite that were not detected in the Nick deposit. The Nick deposit, however, contains monazite, phlogopite, albite, U-phosphate and xenotime that were not detected in the Niutitang samples.

Enrichment factor patterns are highly similar in Zunyi and Sancha, but are different from the enrichment pattern in the Nick deposit (Fig. 7). The Nick deposit appears to be more enriched in Ni than Zunyi and Sancha (EF 4 times greater than EF in Zunyi and 12 times greater than EF in Sancha) and enriched in Zn (EF 8 times greater than EF in Zunyi and 107 times greater than EF in Sancha). The Nick deposit, however, is more depleted than the Niutitang shales in Cu, Se, U and P. This low enrichment in P in the Nick deposit, in comparison with the Niutitang shales, is consistent with the absence of phosphorite nodules observed in the Nick sample by XRF mapping. The absence of phosphorite nodules in the Nick deposit sample strongly suggests that, in the Niutitang shales, phosphorite nodules probably played a role in trapping metals after they accumulated in the sediment, but were not directly responsible for these unusual metal enrichments.

The REE distributions normalised to PAAS show a strong similarity between the Niutitang mineralised layer and the Nick deposit (Fig. 9). Similar to Zunyi and Sancha, the Nick deposit presents a positive Y anomaly, also observed in seawater samples. The Nick deposit is also depleted in light-REE, similar to the Niutitang and seawater samples. It also shows a strong negative Ce anomaly, similar to the one observed for the modern seawater. In addition, the noteworthy congruency of the PGE patterns of the Niutitang black shales and the Nick deposit showing

Table 4
Comparison of different characteristics from Zunyi, Sancha and the Nick deposit.

	Zunyi	Sancha	Nick deposit
Redox conditions	Euxinic conditions	Euxinic conditions	Euxinic conditions
Metal enrichment factors	High enrichment in As, Cu, Mo, P, Se, Ni	Enrichment pattern highly similar to the one in Zunyi. Slight differences include: Ag, As, Cu, Ni more enriched in Zunyi and U, V more enriched in Sancha	More enriched in Ni, Zn and less enriched in Cu, Se and U. No enrichment in P
PGE patterns	Seawater pattern – 4 orders of magnitude enrichment	Seawater pattern – 4 orders of magnitude enrichment	Seawater pattern – 4 orders of magnitude enrichment
REE	Depleted light-REE, slight positive Eu anomaly, positive Y anomaly. Strong similarity with Tokyo Bay pattern – 7 to 8 orders of magnitude enrichment	Depleted light-REE, positive Y anomaly, negative Eu anomaly. Strong similarity with Tokyo Bay pattern – 7 to 8 orders of magnitude enrichment	Depleted light-REE, positive Y anomaly and negative Ce anomaly. Strong similarity with seawater pattern – 7 to 8 orders of magnitude enrichment
Elemental spatial associations	Abundant phosphorite nodules. Brecciated textures	Abundant phosphorite nodules. Brecciated textures	Abundant sulphide lenses with accumulation of Zn and Cu on the edges. Absence of phosphorite nodules

a similar pattern to seawater (Fig. 8) suggest similar mineralisation processes for both mineralisation styles, most likely with a strong contribution from seawater.

5.6. Organic matter and metal accumulation

Sapropels are modern examples of metal accumulation in organic matter-rich sediments, and as such, are possible analogues to the metalliferous black shales reported here. The sapropels of the Eastern Mediterranean, for instance, were deposited under widespread anoxic conditions resulting from water column stagnation and high bioproductivity in the upper water (Nijenhuis et al., 1998; Rohling et al., 2015). These conditions were potentially similar to the ones associated with the South China shales deposition. The thickness of the sapropel layer varies between 8 and 16 cm, it is enriched in numerous elements and it contains up to 27% TOC, with averages between 8 and 12%. Although no obvious increase in Zn concentration was reported, these sapropel layers contain up to 297 ppm As, 1400 ppm Ba, 88 ppm Cd, 206 ppm, Co, 414 ppm Cr, 378 ppm Cu, 728 ppm Mo, 727 ppm Ni, 44 ppm Se and 3575 ppm V (Nijenhuis et al., 1998). Interestingly, the accumulation in these elements is quite heterogeneous within a single sapropel layer with zones enriched in As, Ba, Sb and Se and others rich in Cd, Cr, Cu, Ni and Mo and greater abundance of S. Co and V, however, are distributed evenly throughout the layer (Nijenhuis et al., 1998). These uneven distributions of elements suggest the presence of factors controlling the distribution of metals at μm-scale.

Organic matter can play a significant role in metal transport and accumulation. Organic molecules can react with metal and sulphur species through redox processes and can strongly influence physicochemical properties that control mineralisation and metal distributions (Greenwood et al., 2013 and references therein; Püttmann et al., 1988). In South China, it appears that mineralised shales from Zunyi and Sancha were both deposited under euxinic conditions (Fig. 13). However, comparison with barren shales from above and below the mineralisation (Fig. 13) also highlighted than the barren shales were likewise deposited under euxinic conditions. Evidently the presence of euxinia, although essential to metal accumulation, was not sufficient for the mineralisation. However, microtextural evidence presented above indicates that organic matter played a major role in controlling the final grain-scale disposition of metals in the mineralised layer. To understand the precise role of organic matter in the initial concentration, it is necessary to consider the differences between mineralised and barren shales at the same localities.

In the present study, both barren and mineralised shales show high TOC values (up to 7 wt% for the mineralised shales and up to 13 wt% for the barren shales) and similarly low S1 values (0–1) and no measurable S2. However, a detailed characterisation of organic matter conducted by Kříbek et al. (2007) on barren and mineralised shales revealed that only one type of organic particle was present in the barren shales, although three types of organic particles were identified in the mineralised layer. The first type of particles, present in both the barren and mineralised shales, resembles bituminite macerals often found in coals. It is indicative of a planktonic "rain" containing products of algae, zooplankton and bacterial lipids that were reworked at the sediment/water boundary and within the sediment (Kříbek et al., 2007; Steiner et al., 2001). An additional particle type reported by Kříbek et al. (2007) is exclusively present in the mineralised layer. These particles are mainly present in voids of the sulphidised mineralised layer and represent solidified products of oil migration (migrabitumen). The porous structure of this mineralised layer most likely led to this accumulation of petroleum products during the late stages of diagenesis or catagenesis. The last type of particles identified in the Kříbek et al. (2007) study is also exclusive to the mineralised layer. These rounded particles, mostly found in phosphate grains and sulphide pellets, are likely remnants of algal oncolites. Murowchick et al. (1994) also proposed that phosphorite nodules and sulphidised clasts could have derived from microbial mats of prokaryotic organisms, further highlighting the strong biogenic component of this mineralised layer.

In addition, the complex mixture of MoSC identified in the mineralised layer, potentially assigned to a mixture of nanocrystalline molybdenite (MoS_2) with graphite (Orberger et al., 2007), is also of interest. At the nanoscale, MoSC contains nanometric porous rounded structures of molybdenite that are finely intergrown with organic matter and previous TEM imaging of the MoSC mixture also revealed circular structures presenting striking similarity with bacterial cells (Kao et al., 2001).

Furthermore, a study conducted by Cao et al. (2013) on barren and mineralised shales revealed the presence of organic clots exclusive to the mineralised layer. The authors suggested that the clot morphology resemble that of modern red algae (Rhodophyta) that tend to thrive in reducing conditions due to their higher tolerance to iron limitation (Kelly et al., 2011; Tulipani et al., 2015). In addition, a preferential accumulation of Ni and Mo was highlighted, with higher Mo content in the outer part of the cystocarp and greater Ni abundance in the inner part. An additional study by Strezov and Nonova (2009) compared metal contents in red, brown and green algae from the Black Sea. The results highlighted that species of red algae (Rhodophyta) accumulated more metals (Cd, Cr, Cu, Mn, Pb, Zn) than green and brown algae.

These results tend to suggest that the organic matter could have played a strong role in the accumulation of specific elements. The studies by Kříbek et al. (2007) and Cao et al. (2013), in particular, revealed particle types and organic clots that were exclusive to the mineralised layer. These findings suggest that the organic matter deriving from organisms present in the water column at the time of deposition of the mineralised layer in South China could have had specific characteristics, favouring metal trapping and accumulation in the

sediment. Scott et al. (2017) recently proposed extreme accumulations of H_2S combined with intense activity of phototrophic sulphide-oxidising bacteria in the water column to explain the elevated TOC values and metal hyperenrichment of the Bakken Formation, USA. They suggested that the activity of these bacteria could have led to the production of polysulphides that can form stable complexes with metals (Chadwell et al., 2001).

Organic material was also detected in the Nick deposit sample. First, the lack of brecciation in the Nick deposit (Figs. 11 and 12) could be potentially attributed to the presence of soft and flexible microbial mats that developed shortly after sedimentation and prior to lithification. Such microbial mats could influence localized biogeochemical cycles and promote metal accumulation (Davison et al., 1997; Pagès et al., 2014b). Microscopic investigations of the Nick deposit sample also revealed the presence of composite cells from woody material (Fig. 10). The Late Devonian was characterised by the appearance of tree-plants like such as of *Archaeopteris* that had evolved by the Frasnian and arborescent lycopods such as *Cyclostigma* and *Lepidendropsis*, and the cladoxylalean fern *Rhacophyton* (Algeo et al., 2000). Wood cells in petrified wood have previously shown to be replaced by various minerals including calcite, sphalerite and pyrite (Nowak et al., 2005). In the present study, the woody material had been replaced by pyrite and vaesite, therefore supporting that organic-inorganic chemical interactions were taking place in the Nick mineralised layer.

6. Conclusions

The present study reports, for the first time, a detailed comparison in terms of geochemistry and μm-scale metal distributions and associations in the sulphide polymetallic horizon for two widely separated sites in the Niutitang Formation located hundreds of km apart and for the Nick deposit. The comparison between the two South China sites highlights strong similarities in metal enrichment factors, and PGE distributions, similar to that of seawater. The REE patterns of Sancha and Zunyi also present strong similarities with REE patterns from the Tokyo Bay (restricted environment), although the REE in Zunyi and Sancha are 7 to 8 times more enriched than in seawater samples. High-resolution XRF mapping highlighted brecciated structures and abundant phosphorite nodules in samples from both sites. The highly heterogeneous metal distributions with variations at μm-scale are most likely related to intense variations in redox conditions in the sediment.

Additional comparison was undertaken with the Nick deposit, Canada, regarded as the best analogue of the Niutitang metalliferous shales. This comparison highlights a stronger enrichment in Ni and Zn in the Nick deposit and a greater abundance of minerals in the Niutitang shales. High-resolution XRF mapping and synchrotron-based XRF mapping revealed that the Nick deposit sample does not appear as brecciated as the South China samples and that P is much less abundant. The lack of brecciation is the Nick deposit could be potentially attributed to the presence of soft and flexible microbial mats that developed shortly after sedimentation and prior to lithification. The identification of remineralised plant-derived material in the Nick deposit further emphasizes the potential role of organic matter into metal accumulation in these metalliferous shales. The PGE and REE distributions of both the Nick deposit and the Niutitang shales present highly similar patterns, comparable to that of seawater. A key observation is that phosphorites play a significant role in the detailed micron-scale disposition of elements within the Niutitang polymetallic layer, but are absent at the Nick deposit, where other organic components including fossil wood are present. Phosphorites were evidently important in the final disposition of elements at sub-mm scale at Niutitang but did not play a major role in metal accumulation on the scale of the mineralised layer as a whole.

The present study provides further insight into mineralisation style and processes in these mineralised black shales, highlighting the importance of redox conditions and re-emphasizing the significance of the geological context and the likely role of organic matter in the formation of these mineralised horizons.

Acknowledgments

The synchrotron X-ray fluorescence maps were collected on the X-ray fluorescence microscopy beam line at the Australian Synchrotron, part of ANSTO, and we acknowledge the assistance of Chris Ryan, Margaux Le Vaillant, Daryl Howard, David Paterson and Martin De Jonge. We acknowledge financial support for this facility from the Science and Industry Endowment Fund (SIEF). We also acknowledge financial support from the strategic Priority Research Program (B) of Chinese Academy of Sciences (Grant No. XDB18000000) and Open fund of SKLODG (State Key Lab of Ore Deposit Geochemistry). The authors wish to thank the internal CSIRO reviewers for their constructive comments. Thoughtful reviews by Bernd Lehmann and an anonymous referee helped to improve the manuscript.

References

Algeo, T.J., Maynard, J.B., 2004. Trace-element behavior and redox facies in core shales of Upper Pennsylvanian Kansas-type cyclothems. Chem. Geol. 206, 289–318. http://dx.doi.org/10.1016/j.chemgeo.2003.12.009.

Algeo, T.J., Tribovillard, N., 2009. Environmental analysis of paleoceanographic systems based on molybdenum? Uranium covariation. Chem. Geol. 268, 211–225. http://dx.doi.org/10.1016/j.chemgeo.2009.09.001.

Algeo, T.J., Scheckler, S.E., Maynard, J.B., 2000. Effects of the Middle to Late Devonian spread of vascular land plants on weathering regimes, marine biota, and global climate. In: Gensel, P.G., Edwards, D. (Eds.), 2001 Plants Invade the Land: Evolutionary and Environmental Approaches. Columbia Univ. Press, New York, pp. 213–236.

Barnes, S.J., Liu, W., 2012. Pt and Pd mobility in hydrothermal fluids: evidence from komatiites and from thermodynamic modelling. Ore Geol. Rev. 44, 49–58. http://dx.doi.org/10.1016/j.oregeorev.2011.08.004.

Bau, M., 1991. Rare-earth element mobility during hydrothermal and metamorphic fluid-rock interaction and the significance of the oxidation state of europium. Chem. Geol. 93, 219–230. http://dx.doi.org/10.1016/0009-2541(91)90115-8.

Calvert, S.E., Pedersen, T.F., 1993. Geochemistry of recent oxic and anoxic marine sediments: implications for the geological record. Mar. Geol. 113, 67–88.

Cao, J., Hu, K., Zhou, J., Shi, C., Bian, L., Yao, S., 2013. Organic clots and their differential accumulation of Ni and Mo within early Cambrian black-shale-hosted polymetallic Ni-Mo deposits, Zunyi, South China. J Asian Earth Sci 62, 531–536. http://dx.doi.org/10.1016/j.jseaes.2012.11.002.

Chadwell, S.J., Rickard, D., Luther III, G.W., 2001. Electrochemical evidence for metal polysulfide complexes: tetrasulfide (S42 −) reactions with Mn2 +, Fe2 +, Co2 +, Ni2 +, Cu2 + and Zn2 +. Electroanalysis 13, 21–29.

Coveney, R.M., Nansheng, C., 1991. Ni-Mo-PGE-Au-rich ores in Chinese black shales and speculations on possible analogues in the United States. Miner. Depos. 26, 83–88. http://dx.doi.org/10.1007/BF00195253.

Coveney, R., Grouch, R., Murowchick, J., 1994. Metals, phosphate and stone coal in the Proterozoic and Cambrian of China; the geologic setting of precious metal-bearing Ni-Mo ore beds. SEG Newslett. 18, 1–11.

Davison, W., Fones, G.R., Grime, G.W., 1997. Dissolved metals in surface sediment and a microbial mat at 100-μm resolution. Nature 387, 885–888. http://dx.doi.org/10.1038/43147.

Emsbo, P., Hofstra, A.H., Johnson, C.A., Koenig, A., Grauch, R., Zhang, X., Hu, R., Su, W., Pi, D., 2005. Lower cambrian metallogenesis of south China: interplay between diverse basinal hydrothermal fluids and marine chemistry. In: Mineral Deposit Research: Meeting the Global Challenge. Springer, Berlin Heidelberg, Berlin, Heidelberg, pp. 115–118. doi:10.1007/3-540-27946-6_30.

Filippelli, G.M., 2008. Importance of Phosphorus—Why P? 89–95. doi:10.2113/GSELEMENTS.4.2.89.

Froelich, P., Arthur, M., Burnett, W., Deakin, M., Hensley, V., Jahnke, R., Kaul, L., Kim, K.-H., Roe, K., Soutar, A., Vathakanon, C., 1988. Early diagenesis of organic matter in Peru continental margin sediments: phosphorite precipitation. Mar. Geol. 80, 309–343. http://dx.doi.org/10.1016/0025-3227(88)90095-3.

Goodfellow, W., 2007. Base metal metallogeny of the Selwyn Basin, Canada, in Mineral Deposits of Canada: a synthesis of major deposit-types, district metallogeny, the evolution of geological provinces, and exploration methods. Geol. Assoc. Canada, Miner. Depos. Div. Spec. Publ. 5, 553–579.

Goodfellow, W.D., Geldsetzer, H., Gregoire, C., Orchard, M., Cordey, F., 2010. TGI-3 Workshop: Public geoscience in support of base metal exploration programme and abstracts. Geol. Assoc. Canada, Cordilleran Sec. 2010, 15–18.

Greenwood, P.F., Brocks, J.J., Grice, K., Schwark, L., Jaraula, C.M.B., Dick, J.M., Evans, K.A., 2013. Organic geochemistry and mineralogy. I. Characterisation of organic matter associated with metal deposits. Ore Geol. Rev. 50, 1–27. http://dx.doi.org/10.1016/j.oregeorev.2012.10.004.

Hatch, J.R., Leventhal, J.S., 1992. Relationship between inferred redox potential of the depositional environment and geochemistry of the Upper Pennsylvanian (Missourian) stark shale member of the Dennis Limestone, Wabaunsee country, Kansas, USA. Chem. Geol. 99, 65–82.

Horan, M., Morgan, J., Grauch, R., Coveney, J.R., Murowchick, J., Hulbert, L., 1994. Rhenium and osmium isotopes in black shales and Ni–Mo–PGE-rich sulfide layers, Yukon Territory, Canada, and Hunan and Guizhou Provinces, China. Geochim. Cosmochim. Acta 58, 257–265.
Hulbert, L.J., Carne, R.C., Gregoire, D.C., Paktunc, D., 1992. Sedimentary nickel, zinc, and platinum-group-element mineralization in Devonian black shales at the Nick Property, Yukon, Canada; a new deposit type. Explor. Min. Geol. 1.
Jiang, S.-Y., Chen, Y.-Q., Ling, H.-F., Yang, J.-H., Feng, H.-Z., Ni, P., 2006. Trace- and rare-earth element geochemistry and Pb-Pb dating of black shales and intercalated Ni-Mo-PGE-Au sulfide ores in Lower Cambrian strata, Yangtze Platform, South China. Miner. Depos. 41, 453–467. http://dx.doi.org/10.1007/s00126-006-0066-6.
Jones, B., Manning, D.A.C., 1994. Comparison of geochemical indices used for the interpretation of palaeoredox conditions in ancient mudstones. Chem. Geol. 111, 111–129. http://dx.doi.org/10.1016/0009-2541(94)90085-X.
Jowitt, S.M., Keays, R.R., 2011. Shale-hosted Ni–(Cu–PGE) mineralisation: a global overview. Appl. Earth Sci. 1204, 187–197. http://dx.doi.org/10.1179/1743275812Z.00000000026doi.org/10.1179/1743275812Z.00000000026.
Kao, L.S., Peacor, D.R., Coveney, J., Zhao, G., Dungey, K.E., Curtis, M.D., Penner-Hahn, J.E., 2001. A C/MoS2 mixed-layer phase (MoSC) occurring in metalliferous black shales from Southern China, and new data on jordisite. Am. Mineral. 86, 852–861.
Kelly, A.E., Love, G.D., Zumberge, J.E., Summons, R.E., 2011. Hydrocarbon biomarkers of Neoproterozoic to Lower Cambrian oils from eastern Siberia. Org. Geochem. 42, 640–654. http://dx.doi.org/10.1016/j.orggeochem.2011.03.028.
Kidder, D.L., Krishnaswamy, R., Mapes, R.H., 2003. Elemental mobility in phosphatic shales during concretion growth and implications for provenance analysis. Chem. Geol. 198, 335–353. http://dx.doi.org/10.1016/S0009-2541(03)00036-6.
Kirkham, R., Dunn, P.A., Kuczewski, A.J., Siddons, D.P., Dodanwela, R., Moorhead, G.F., Ryan, C.G., De Geronimo, G., Beuttenmuller, R., Pinelli, D., Pfeffer, M., Davey, P., Jensen, M., Paterson, D.J., de Jonge, M.D., Howard, D.L., Küsel, M., McKinlay, J., Garrett, R., Gentle, I., Nugent, K., Wilkins, S., 2010. The Maia spectroscopy detector system: engineering for integrated pulse capture, low-latency scanning and real-time processing. In: AIP Conference Proceedings. pp. 240–243. doi:10.1063/1.3463181.
Kříbek, B., Sýkorová, I., Pašava, J., Machovič, V., 2007. Organic geochemistry and petrology of barren and Mo–Ni–PGE mineralized marine black shales of the Lower Cambrian Niutitang Formation (South China). Int. J. Coal Geol. 72, 240–256. http://dx.doi.org/10.1016/j.coal.2007.02.002.
Lehmann, B., Mao, J.W., Li, S.R., Zhang, G.D., 2003. Re–Os dating of polymetallic Ni–Mo–PGE–Au mineralization in Lower Cambrian black shales of South China and its geological significance — A reply. Econ. Geol. 98, 663–665.
Lehmann, B., Nägler, T.F., Wille, M., Dulski, P., 2007. Highly metalliferous carbonaceous shale and Early Cambrian seawater. Geology 403–406. http://dx.doi.org/10.1130/G23543A.1.
Lehmann, B., Frei, R., Xu, L., Mao, J., 2016. Early Cambrian black shale-hosted Mo-Ni and V mineralization on the rifted margin of the Yangtze platform, China: Reconnaissance chromium isotope data and a refined metallogenic model. Econ. Geol. 111, 89–103. http://dx.doi.org/10.2113/econgeo.111.1.89.
Li, S.R., Gao, Z.M., 1996. Silicalite of hydrothermal origin in the Lower Cambrian black rock series of South China. Acta Miner. Sin. 16, 416–422 (in Chinese with English abstract).
Liu, W., Etschmann, B., Migdisov, A., Boukhalfa, H., Testemale, D., Müller, H., Hazemann, J.-L., Brugger, J., 2017. Revisiting the hydrothermal geochemistry of europium(II/III) in light of new in-situ XAS spectroscopy results. Chem. Geol. 459, 61–74. http://dx.doi.org/10.1016/j.chemgeo.2017.04.005.
Lott, D.A., Coveney, R.M., Murowchick, J.B., Grauch, R.I., 1999. Sedimentary exhalative nickel-molybdenum ores in South China. Econ. Geol. 94.
MacRae, N.D., Nesbitt, H.W., Kronberg, B.I., 1992. Development of a positive Eu anomaly during diagenesis. Earth Planet. Sci. Lett. 109, 585–591. http://dx.doi.org/10.1016/0012-821X(92)90116-D.
Mao, J., Lehmann, B., Du, A., Zhang, G., Ma, D., Wang, Y., Zeng, M., Kerrich, R., 2002. Re-Os dating of polymetallic Ni-Mo-PGE-Au mineralization in Lower Cambrian Black Shales of South China and its geologic significance. Econ. Geol. 97, 1051–1061. http://dx.doi.org/10.2113/gsecongeo.97.5.1051.
Martinez-Ruiz, F., Ortega-Huertas, M., Palomo, I., 1999. Positive Eu anomaly development during diagenesis of the K/T boundary ejecta layer in the Agost section (SE Spain): implications for trace-element remobilization. Terra Nova 11, 290–296. http://dx.doi.org/10.1046/j.1365-3121.1999.00261.x.
Morse, J.W., Luther, G.W., 1999. Chemical influences on trace metal-sulfide interactions in anoxic sediments. Geochim. Cosmochim. Acta 63, 3373–3378. http://dx.doi.org/10.1016/S0016-7037(99)00258-6.
Murowchick, J.B., Coveney, R.M., Grauch, R.I., Eldridge, C.S., Shelton, K.L., 1994. Cyclic variations of sulfur isotopes in Cambrian stratabound Ni-Mo-(PGE-Au) ores of southern China. Geochim. Cosmochim. Acta 58, 1813–1823. http://dx.doi.org/10.1016/0016-7037(94)90538-X.
Nijenhuis, I., Brumsack, H.-J., de Lange, G., 1998. The trace element composition of organic carbon-rich sapropels versus black shales: a comparison. In: A.H.F. Robertson, K.-C. Emeis, C. Richter, A. Camerlenghi (Eds.), Proc. ODP, Sci. Res. 160. College Station, TX (Ocean Drilling Program). pp. 199–206.
Nowak, J., Florek, M., Kwiatek, W., Lekki, J., Chevallier, P., Zięba, E., Mestres, N., Dutkiewicz, E.M., Kuczumow, A., 2005. Composite structure of wood cells in petrified wood. Mater. Sci. Eng. C 25, 119–130. http://dx.doi.org/10.1016/j.msec.2005.01.018.
Nozaki, Y., 1997. A fresh look at element distribution in the North Pacific Ocean. Eos Trans. Am. Geophys. Union 78http://dx.doi.org/10.1029/97EO00148. 221–221.
Nozaki, Y., Zhang, J., 1995. The rare earth elements and yttrium in the coastal/offshore mixing zone of Tokyo Bay waters and the Kuroshio. Biogeochem. Process. Ocean Flux West. Pac. 171–184.
Orberger, B., Pasava, J., Galien, J., Daudin, L., Pinti, D.L., 2003. Geochemical exploration. J. Geochem. Explor. 79, 215–219. http://dx.doi.org/10.1016/S0375.
Orberger, B., Vymazalova, A., Wagner, C., Fialin, M., Gallien, J.P., Wirth, R., Pasava, J., Montagnac, G., 2007. Biogenic origin of intergrown Mo-sulphide- and carbonaceous matter in Lower Cambrian black shales (Zunyi Formation, southern China). Chem. Geol. 238, 213–231. http://dx.doi.org/10.1016/j.chemgeo.2006.11.010.
Pagès, A., Welsh, D.T., Teasdale, P.R., Grice, K., Vacher, M., Bennett, W.W., Visscher, P.T., 2014a. Diel fluctuations in solute distributions and biogeochemical cycling in a hypersaline microbial mat from Shark Bay, WA. Mar. Chem. 167, 102–112. http://dx.doi.org/10.1016/j.marchem.2014.05.003.
Pagès, A., Grice, K., Vacher, M., Welsh, D.T., Teasdale, P.R., Bennett, W.W., Greenwood, P., 2014b. Characterizing microbial communities and processes in a modern stromatolite (Shark Bay) using lipid biomarkers and two-dimensional distributions of porewater solutes. Environ. Microb. 16, 2458–2474. http://dx.doi.org/10.1111/1462-2920.12378.
Pagès, A., Grice, K., Welsh, D.T., Teasdale, P.T., Van Kranendonk, M.J., Greenwood, P., 2015. Lipid Biomarker and Isotopic Study of Community Distribution and Biomarker Preservation in a Laminated Microbial Mat from Shark Bay, Western Australia. Microb. Ecol. 70, 459–472. http://dx.doi.org/10.1007/s00248-015-0598-3.
Pasăva, J., 1993. Anoxic sediments – an important environment for PGE; an overview. Ore Geol. Rev. 8, 425–445. http://dx.doi.org/10.1016/0169-1368(93)90037-Y.
Pašava, J., Kříbek, B., Vymazalová, A., Sýkorová, I., Žák, K., Orberger, B., 2008. Multiple sources of metals of mineralization in Lower Cambrian Black Shales of South China: evidence from geochemical and petrographic study. Resour. Geol. 58, 25–42. http://dx.doi.org/10.1111/j.1751-3928.2007.00042.x.
Patterson, J.H., Ramsden, A.R., Dale, L.S., Fardy, J.J., 1986. Geochemistry and mineralogical residences of trace elements in oil shales from Julia Creek, Queensland, Australia. Chem. Geol. 55, 1–16. http://dx.doi.org/10.1016/0009-2541(86)90123-3.
Pi, D., Liu, C., Shields-zhou, G.A., Jiang, S., 2013. Trace and rare earth element geochemistry of black shale and kerogen in the early Cambrian Niutitang Formation in Guizhou province, South China: constraints for redox environments and origin of metal enrichments. Precambr. Res. 225, 218–229. http://dx.doi.org/10.1016/j.precamres.2011.07.004.
Piper, D.Z., Perkins, R.B., 2004. A modern vs. Permian black shale—the hydrography, primary productivity, and water-column chemistry of deposition. Chem. Geol. 206, 177–197. http://dx.doi.org/10.1016/j.chemgeo.2003.12.006.
Püttmann, W., Hagemann, H.W., Merz, C., Speczik, S., 1988. Influence of organic material on mineralization processes in the Permian Kupferschiefer formation, Poland. Org. Geochem. 13, 357–363. http://dx.doi.org/10.1016/0146-6380(88)90056-3.
Reinhard, C.T., Planavsky, N.J., Gill, B.C., Ozaki, K., Robbins, L.J., Lyons, T.W., Fischer, W.W., Wang, C., Cole, D.B., Konhauser, K.O., 2017. Evolution of the global phosphorus cycle. Nature 541, 386–389. http://dx.doi.org/10.1038/nature20772.
Rohling, E.J., Marino, G., Grant, K.M., 2015. Mediterranean climate and oceanography, and the periodic development of anoxic events (sapropels). Earth Sci. Rev. 143, 62–97.
Ryan, C.G., Siddons, D.P., Kirkham, R., Dunn, P.A., Kuczewski, A., Moorhead, G., De Geronimo, G., Paterson, D.J., de Jonge, M.D., Hough, R.M., Lintern, M.J., Howard, D.L., Kappen, P., Cleverley, J., Denecke, M., Walker, C.T., 2010. The New Maia Detector System: methods for high definition trace element imaging of natural material. AIP Conf. Proc. 9–17. http://dx.doi.org/10.1063/1.3399266.
Scott, C., Kelley, K.D., Slack, J.F., 2014. The geobiology of sediment-hosted mineral deposits. In: In: Kelley, K.D., Golden, H.C. (Eds.), Building Exploration Capability for the 21st Century, vol. 18. Society Economic Geologists Spec. Publ., pp. 17–35.
Scott, C.T., Slack, J.F., Kelley, K.D., 2017. The hyper-enrichment of V and Zn in black shales of the late devonian-early Mississippian Bakken formation (USA). Chem. Geol. 452, 24–33.
Seaman, J.C., Arey, J.S., Bertsch, P.M., 2001. Immobilization of nickel and other metals in contaminated sediments by hydroxyapatite addition. J. Environ. Qual. 30, 460. http://dx.doi.org/10.2134/jeq2001.302460x.
Slansky, M., 1986. Geology of Sedimentary Phosphates. Elsevier Science Pub. Co., Inc., New York, NY.
Steiner, M., Wallis, E., Erdtmann, B.D., Zhao, Y., Yang, R., 2001. Submarine-hydrothermal exhalative ore layers in black shales from South China and associated fossils – insights into a Lower Cambrian facies and bio-evolution. Palaeogeogr. Palaeoclimatol. Palaeoecol. 169, 165–191. http://dx.doi.org/10.1016/S0031-0182(01)00208-5.
Strezov, A., Nonova, T., 2009. Influence of macroalgal diversity on accumulation of radionuclides and heavy metals in Bulgarian Black Sea ecosystems. J. Environ. Radioact. 100, 144–150. http://dx.doi.org/10.1016/j.jenvrad.2008.09.007.
Sverjensky, D.A., 1984. Europium redox equilibria in aqueous solution. Earth Planet. Sci. Lett. 67, 70–78. http://dx.doi.org/10.1016/0012-821X(84)90039-6.
Taylor, S.R., McLennan, S.M., 1985. The continental crust: its composition and evolution. Blackwell, Malden, Mass.
Tribovillard, N., Algeo, T.J., Lyons, T., Riboulleau, A., 2006. Trace metals as paleoredox and paleoproductivity proxies: an update. Chem. Geol. 232, 12–32. http://dx.doi.org/10.1016/j.chemgeo.2006.02.012.
Tribovillard, N., Algeo, T.J., Baudin, F., Riboulleau, A., 2012. Analysis of marine environmental conditions based on molybdenum? Uranium covariation? Applications to mesozoic paleoceanography. Chem. Geol. 324–325, 46–58. http://dx.doi.org/10.1016/j.chemgeo.2011.09.009.
Tulipani, S., Grice, K., Greenwood, P.F., Haines, P.W., Sauer, P.E., Schimmelmann, A., Summons, R.E., Foster, C.B., Böttcher, M.E., Playton, T., Schwark, L., 2015. Changes of palaeoenvironmental conditions recorded in Late Devonian reef systems from the Canning Basin, Western Australia: a biomarker and stable isotope approach. Gondwana Res. 28, 1500–1515. http://dx.doi.org/10.1016/j.gr.2014.10.003.
Tyson, R.V., Pearson, T.H., 1991. Modern and ancient continental shelf anoxia: an overview. In: Tyson, R.V., Pearson, T.H. (Eds.), Modern and Ancient Continental

Shelf Anoxia. Geol. Soc. London, Spec. Publ., No. 58, pp. 1–24.
Van Cappellen, P., Berner, R., 1988. A mathematical model for the early diagenesis of phosphorus and fluorine in marine sediments. Apatite precipitation. Am. J. Sci. 288, 289–333.
Wagner, M., Chappaz, A., Lyons, T., 2017. Molybdenum speciation and burial pathway in weakly sulfidic environments: insights from XAFS. Geochim. Cosmochim. Acta 206, 18–29.
Wanty, R.B., Goldhaber, M.B., 1992. Thermodynamics and kinetics of reactions involving vanadium in natural systems: accumulation of vanadium in sedimentary rocks. Geochim. Cosmochim. Acta 56, 1471–1483.
Wilby, P.R., Briggs, D.E.G., Bernier, P., Gaillard, C., 1996. Role of microbial mats in the fossilization of soft tissues. Geology 24, 787. http://dx.doi.org/10.1130/0091-7613(1996) 024<0787:ROMMIT>2.3.CO;2.
Xu, L., Lehmann, B., Mao, J., Nägler, T.F., Neubert, N., Böttcher, M.E., Escher, P., 2012. Mo isotope and trace element patterns of Lower Cambrian black shales in South China: multi-proxy constraints on the paleoenvironment. Chem. Geol. 318–319, 45–59. http://dx.doi.org/10.1016/j.chemgeo.2012.05.016.
Xu, L., Lehmann, B., Mao, J., 2013. Seawater contribution to polymetallic Ni–Mo–PGE–Au mineralization in Early Cambrian black shales of South China: evidence from Mo isotope, PGE, trace element, and REE geochemistry. Ore Geol. Rev. 52, 66–84. http://dx.doi.org/10.1016/j.oregeorev.2012.06.003.
Yin, R., Xu, L., Lehmann, B., Lepak, R.F., Hurley, J.P., Mao, J., Feng, X., Hu, R., 2017. Anomalous mercury enrichment in Early Cambrian black shales of South China: mercury isotopes indicate a seawater source. Chem. Geol. 467, 159–167. http://dx.doi.org/10.1016/j.chemgeo.2017.08.010.
Zeng, M., 1998. Geological characteristics of the Huangjiawan Mo-Ni deposit and its development in the future. Guizhou Geol. 15, 305–310.
Zhu, M.-Y., Zhang, J.-M., Steiner, M., Yang, A., Li, G.-X., Erdtmann, B.-D., 2003. Sinian-Cambrian stratigraphic framework for shallow to deep-water environments of the Yangtze Platform: an integrated approach. Prog. Nat. Sci. 13, 946–950.